# Understanding the extreme luminosity of DES14X2fna

M. Grayling [1,2]★ C. P. Gutiérrez [1], M. Sullivan [1], P. Wiseman [1], M. Vincenzi [3],
S. González-Gaitán [4], B. E. Tucker,[5] L. Galbany [6], L. Kelsey [1], C. Lidman [5], E. Swann,[3]
M. Smith [1], C. Frohmaier, D. Carollo,[7] K. Glazebrook,[8] G. F. Lewis [9], A. Möller,[10] S. R. Hinton [11],
S. A. Uddin,[12] T. M. C. Abbott,[13] M. Aguena [14,15] S. Avila [16], E. Bertin [17,18] S. Bhargava,[19]
D. Brooks,[20] A. Carnero Rosell [21,22] M. Carrasco Kind [23,24] J. Carretero [25], M. Costanzi,[26,27]
L. N. da Costa,[15,28] J. De Vicente [29], S. Desai,[30] H. T. Diehl,[31] P. Doel,[20] S. Everett,[32] I. Ferrero [33],
P. Fosalba [34,35] J. Frieman,[31,36] J. García-Bellido [16], E. Gaztanaga [34,35] D. Gruen [37,38,39] R.
A. Gruendl,[23,24] J. Gschwend,[15,28] G. Gutiérrez [31] B. Hoyle,[40,41,42] K. Kuehn,[43,44] N. Kuropatkin,[31]
M. Lima,[14,15] N. MacCrann [45,46] J. L. Marshall,[47] P. Martini,[45,48,49] R. Miquel,[25,50] R. Morgan,[51]
A. Palmese [31,36] F. Paz-Chinchón,[24,52] A. A. Plazas [53] A. K. Romer,[19] C. Sánchez [54] E. Sanchez,[29]
V. Scarpine,[31] S. Serrano,[34,35] I. Sevilla-Noarbe,[29] M. Soares-Santos [55] E. Suchyta [56] G. Tarle,[55]
D. Thomas [3], C. To [37,38,39] T. N. Varga,[41,42] A. R. Walker,[13] and R. D. Wilkinson[19] (DES Collaboration)

*Affiliations are listed at the end of the paper*

## ABSTRACT

We present DES14X2fna, a high-luminosity, fast-declining Type IIb supernova (SN IIb) at redshift $z = 0.0453$, detected by the Dark Energy Survey (DES). DES14X2fna is an unusual member of its class, with a light curve showing a broad, luminous peak reaching $M_r \simeq -19.3$ mag 20 d after explosion. This object does not show a linear decline tail in the light curve until $\simeq 60$ d after explosion, after which it declines very rapidly ($4.30 \pm 0.10$ mag 100 d$^{-1}$ in the $r$ band). By fitting semi-analytic models to the photometry of DES14X2fna, we find that its light curve cannot be explained by a standard $^{56}$Ni decay model as this is unable to fit the peak and fast tail decline observed. Inclusion of either interaction with surrounding circumstellar material or a rapidly-rotating neutron star (magnetar) significantly increases the quality of the model fit. We also investigate the possibility for an object similar to DES14X2fna to act as a contaminant in photometric samples of SNe Ia for cosmology, finding that a similar simulated object is misclassified by a recurrent neural network (RNN)-based photometric classifier as an SN Ia in $\sim 1.1$–2.4 per cent of cases in DES, depending on the probability threshold used for a positive classification.

**Key words:** supernovae: general – supernovae: individual: DES14X2fna.

## 1 INTRODUCTION

Core-collapse supernovae (SNe) are a diverse and heterogeneous population of events, with the variety of observed sub-types reflecting the complexity of their possible progenitor systems and astrophysics. Type II SNe (SNe II) are events displaying hydrogen lines in their photospheric spectra, SNe Ib lack hydrogen but do contain helium, while SNe Ic lack both. SNe IIb are an intermediate class, displaying hydrogen lines at early times before the appearance of helium lines as seen in SNe Ib (Filippenko 1997; Gal-Yam 2017; Modjaz, Gutiérrez & Arcavi 2019).

The commonly accepted physical explanation for SNe IIb is that their progenitors have had their outer hydrogen envelope partially, but not fully, stripped away. SNe Ib have this envelope fully stripped, leading to spectra with helium but not hydrogen, while

the progenitors of SNe Ic are stripped of both hydrogen and helium. A further class of stripped-envelope SNe, SN Ic with broad lines (SN Ic-BLs), shows similar spectroscopic features to SNe Ic, but with broader features indicating high expansion velocities and an energetic explosion.

The exact mechanism driving the envelope stripping of these SNe is still open for debate, but proposed solutions include stellar winds (Woosley, Langer & Weaver 1993) and interaction with a binary companion (Nomoto, Iwamoto & Suzuki 1995) in the case of a binary progenitor system. Stellar winds require massive progenitors of $\gtrsim 25$–$30 \, M_\odot$ in order to remove at least the majority of the hydrogen envelope (Eldridge & Tout 2004). Pre-explosion and late-time images of the SN environment of the well-studied SN IIb SN 1993J (Aldering, Humphreys & Richmond 1994; Fox et al. 2014) indicate the presence of a binary system, with evidence of a binary companion also found in SN 2001ig (Ryder et al. 2018) and SN 2011dh (Folatelli et al. 2014). However, deep imaging studies of the SN IIb remnant Cassiopeia A have not indicated a binary

★ E-mail: m.j.p.grayling@soton.ac.uk

companion (Kochanek 2018; Kerzendorf et al. 2019), suggesting that both of these progenitor scenarios may occur.

In the canonical picture of an SN IIb, the light curve is driven by the radioactive decay chain of $^{56}$Ni synthesized in the explosion, which subsequently decays into $^{56}$Co and then stable $^{56}$Fe. Treatments of this radioactive decay model, for example, the commonly used 'Arnett' model from Arnett (1982) and more recently Khatami & Kasen (2019), allow for various properties of the explosion to be estimated. Some other types of core-collapse SNe are primarily driven by different physical processes (e.g. interaction with a surrounding circumstellar material (CSM) for SNe IIn; Moriya et al. 2013), although a $^{56}$Ni decay model can still be used to estimate some explosion properties (e.g. Prentice et al. 2016; Meza & Anderson 2020). For SNe with light curves driven by $^{56}$Ni decay such as SNe IIb, a more luminous SN indicates a higher synthesized mass of $^{56}$Ni to power the peak of the light curve.

Energetic SNe Ic-BL, however, are not well fit by this model, which cannot reproduce both the luminous peaks and the late-time light curves of these objects. These objects have traditionally been fit with a two-component model, with the light-curve peak and broad spectral features powered by a fast-moving component and the exponential decline powered by a slower moving dense component (Maeda et al. 2003). However, more recently, magnetar models have also proved successful in fitting the light curves of these objects. In this scenario, the light curve is powered by a combination of radioactive decay and energy injected into the system by a central engine, the spin-down of a rapidly rotating neutron star (Kasen & Bildsten 2010; Woosley 2010). Wang et al. (2017) show that a combination of a magnetar with $^{56}$Ni decay successfully fits the light curves of the SNe Ic-BL SN 1998bw and SN 2002ap, with the magnetar able to explain the deviation of the late-time light curve from the intermediate exponential decline.

In addition to this, some SNe IIb (e.g. 1993J, Richmond et al. 1994; 2016gkg, Arcavi et al. 2017b; Bersten et al. 2018) exhibit an initial peak in their light curves, which has been attributed to post-shock-breakout cooling in the case of a progenitor with a compact core surrounded by extended, low-mass material (Bersten et al. 2012; Nakar & Piro 2014). This typically occurs over a short period of a few days, and is not observed in all SNe IIb (e.g. SN 2008ax; Pastorello et al. 2008), potentially because the SN is not discovered until after this phase. This pre-max bump can help infer properties of the progenitor including radius and binarity using hydrodynamic simulations (e.g. Bersten et al. 2012; Piro 2015; Sapir & Waxman 2017).

As the spectroscopic properties of a stripped-envelope SN differ primarily due to the degree of stripping of the progenitor star, it is an open question as to whether SNe IIb, Ib, Ic, and Ic-BL are distinct classes or part of a continuum (Modjaz et al. 2019). Galbany et al. (2018) find that SNe IIb have unusual host properties compared with other core-collapse SN hosts, having particularly low metallicity and star formation rate (SFR). However, Schulze et al. (2020) finds that the host properties of SNe IIb are consistent with those of SNe II. SNe Ib, Ic and Ic-BL have been previously observed with peak absolute magnitudes from $-16$ up to and even brighter than $-20$, as shown in figs 2 and 3 of Modjaz et al. (2019). Historically, SNe IIb have exhibited less diversity in peak luminosity, ranging from a peak $r/R$-band absolute magnitude of roughly $-16.5$ to $-18$. However, the recent discovery of ASASSN-18am with a peak $M_V \sim -19.7$ (Bose et al. 2020) demonstrated that SNe IIb can reach considerable luminosities.

In this paper, we present photometry and spectroscopy of DES14X2fna, an unusual and very luminous SN IIb discovered by Dark Energy Survey (DES) under the Dark Energy Survey Supernova Programme (DES-SN; Bernstein et al. 2012) and exhibiting very different properties to those shown by previously observed SNe IIb. In Section 2, we detail our observations of DES14X2fna. In Section 3, we analyse the spectroscopic and photometric properties of both the SN and its host, and compare to samples of historic SNe. We consider a variety of semi-analytic models to explain the luminosity and evolution of DES14X2fna in Section 4. Next, we discuss the possible mechanisms that could drive the unusual light curve of DES14X2fna and consider the possibility that a similar object could act as a contaminant in photometric samples of SNe Ia in Section 5, before concluding in Section 6. Throughout this analysis, we have assumed a flat $\Lambda$CDM cosmology with $\Omega_M = 0.3$, $\Omega_\Lambda = 0.7$, and $H_0 = 70$ km s$^{-1}$ Mpc$^{-1}$.

## 2 OBSERVATIONS

DES14X2fna was discovered by DES-SN in an *r*-band image captured by Dark Energy Camera (DECam; Flaugher et al. 2015) at an apparent magnitude of $m_r = 19.1$ mag. This discovery was on 2014 October 1 (MJD 56931.2), with a previous non-detection on 2014 September 24 (MJD 56924.2) at $m_z \sim 23.7$. The transient was located in a faint host galaxy with $M_r \sim -16$ at $z = 0.0453$,[1] at position $\alpha = 02^h23^m15\overset{s}{.}64$, $\delta = -07°05'20\overset{''}{.}8$ (J2000). Based on the epochs of first detection and last non-detection, we adopt an explosion date of MJD $56927.7 \pm 3.5$ d.

After discovery, *griz* photometric coverage was acquired by DES-SN until 2015 January. Photometric measurements were made using the pipeline outlined in Papadopoulos et al. (2015) and Smith et al. (2016), which uses template subtraction to remove the host galaxy contribution to the image using a point spread function (PSF) matching routine. From this difference image, PSF-fitting is used to measure the SN photometry. We correct the photometry for Milky Way extinction using dust maps from Schlafly & Finkbeiner (2011), assuming $R_V = 3.1$. We assume negligible host galaxy extinction – we verify this by comparing H$\alpha$ and H$\beta$ flux ratios in spectroscopy of the host, which we find to be consistent with $E(B - V)_{\text{host}} \sim 0$ (Osterbrock 1989).

Photometric data were then *K*-corrected into the rest frame. We do this using the SED templates of DES14X2fna from Hounsell et al. (in preparation), which we interpolate to epochs where we have observations and calibrate ('mangle') to match our photometry. The mangling process required simultaneous observations in each photometric band – although the DES observations were near simultaneous across different bands, in a few instances, data for a given band were missing. To complete our data and give fully simultaneous data, we interpolate the observed light curves using Gaussian processes (GP; Rasmussen & Williams 2005). These were implemented using the PYTHON package GEORGE (Ambikasaran et al. 2015), following the process outlined in Angus et al. (2019). The observed photometry without any corrections is detailed in Table 1, and the corrected rest-frame light curves are shown in Fig. 1 and also detailed in Table 1. The quoted uncertainties for the observer-frame photometry are purely statistical without incorporating any systematic uncertainties. Due to the high signal-to-noise observations of DES14X2fna, these uncertainties are very small and reach millimag levels at peak. In practice, the uncertainties will be larger than this – for our analysis, we add the statistical errors in quadrature with a value of 0.05 mag to represent systematic uncertainty. This value was selected as the smallest statistical error we could apply to obtain a stable GP fit

---

[1]Obtained from narrow host galaxy emission features.

**Table 1.** Observed and rest-frame photometry of DES14X2fna, quoted in AB magnitudes in the natural DECam system.

| MJD | UT date | Rest-frame phase (d) | g (mag) | (rest) (mag) | r (mag) | (rest) (mag) | i (mag) | (rest) (mag) | z (mag) | (rest) (mag) |
|---|---|---|---|---|---|---|---|---|---|---|
| 56923.3 | 20140923 | −4.2 | >23.7 | – | >23.5 | – | – | – | – | – |
| 56924.2 | 20140924 | −3.3 | >23.9 | – | – | – | >23.9 | – | >23.7 | – |
| 56931.1 | 20141001 | 3.3 | 18.980 ± 0.005 | 18.87 ± 0.07 | 19.13 ± 0.01 | 18.98 ± 0.06 | 19.30 ± 0.01 | 19.14 ± 0.06 | 19.44 ± 0.01 | 19.24 ± 0.05 |
| 56934.4 | 20141004 | 6.4 | 18.115 ± 0.003 | 17.89 ± 0.05 | 18.281 ± 0.004 | 18.06 ± 0.05 | 18.42 ± 0.01 | 18.21 ± 0.05 | 18.60 ± 0.01 | 18.35 ± 0.05 |
| 56936.3 | 20141006 | 8.3 | 17.504 ± 0.002 | 17.51 ± 0.05 | 17.727 ± 0.002 | 17.69 ± 0.05 | 17.911 ± 0.002 | 17.86 ± 0.05 | 18.077 ± 0.003 | 18.02 ± 0.05 |
| 56943.2 | 20141013 | 14.9 | 17.137 ± 0.001 | 17.03 ± 0.05 | 17.278 ± 0.001 | 17.16 ± 0.05 | – | 17.33 ± 0.05 | 17.569 ± 0.002 | 17.39 ± 0.05 |
| 56949.1 | 20141019 | 20.5 | 17.240 ± 0.002 | 17.12 ± 0.05 | 17.291 ± 0.002 | 17.17 ± 0.05 | 17.40 ± 0.01 | 17.28 ± 0.05 | 17.524 ± 0.003 | 17.39 ± 0.05 |
| 56956.2 | 20141026 | 27.3 | 17.655 ± 0.002 | 17.56 ± 0.05 | 17.604 ± 0.002 | 17.47 ± 0.05 | 17.688 ± 0.002 | 17.53 ± 0.05 | 17.782 ± 0.002 | 17.63 ± 0.05 |
| 56960.2 | 20141030 | 31.1 | 17.986 ± 0.002 | 17.92 ± 0.06 | 17.826 ± 0.002 | 17.69 ± 0.05 | 17.906 ± 0.002 | 17.77 ± 0.05 | – | 17.89 ± 0.05 |
| 56973.0 | 20141112 | 43.4 | 19.405 ± 0.005 | 19.43 ± 0.07 | 18.726 ± 0.003 | 18.64 ± 0.06 | 18.716 ± 0.003 | 18.57 ± 0.06 | 18.780 ± 0.004 | 18.67 ± 0.05 |
| 56980.0 | 20141119 | 50.1 | 20.55 ± 0.01 | 20.63 ± 0.07 | 19.57 ± 0.01 | 19.51 ± 0.06 | 19.49 ± 0.01 | 19.37 ± 0.05 | 19.43 ± 0.01 | 19.38 ± 0.05 |
| 56987.1 | 20141126 | 56.8 | 21.53 ± 0.02 | 21.66 ± 0.07 | 20.32 ± 0.01 | 20.25 ± 0.06 | 20.28 ± 0.01 | 20.17 ± 0.06 | 20.08 ± 0.01 | 20.11 ± 0.05 |
| 56990.1 | 20141129 | 59.7 | 21.85 ± 0.14 | 21.95 ± 0.19 | 20.51 ± 0.06 | 20.51 ± 0.08 | 20.51 ± 0.17 | 20.50 ± 0.09 | 20.37 ± 0.04 | 20.35 ± 0.06 |
| 56991.1 | 20141130 | 60.7 | – | 21.84 ± 0.11 | 20.81 ± 0.04 | 20.67 ± 0.06 | 20.73 ± 0.04 | 20.61 ± 0.06 | 20.41 ± 0.04 | 20.41 ± 0.05 |
| 56992.1 | 20141201 | 61.6 | 21.83 ± 0.06 | 21.94 ± 0.10 | 20.65 ± 0.02 | 20.60 ± 0.06 | 20.65 ± 0.02 | 20.57 ± 0.05 | 20.36 ± 0.02 | 20.44 ± 0.05 |
| 57001.3 | 20141210 | 70.4 | 22.46 ± 0.15 | 22.63 ± 0.21 | 21.07 ± 0.03 | 20.99 ± 0.07 | 21.13 ± 0.03 | 21.04 ± 0.06 | 20.72 ± 0.03 | 20.82 ± 0.05 |
| 57005.0 | 20141214 | 74.0 | 22.55 ± 0.08 | 22.72 ± 0.12 | 21.26 ± 0.03 | 21.15 ± 0.07 | – | 21.35 ± 0.07 | – | 21.09 ± 0.06 |
| 57005.1 | 20141214 | 74.1 | – | – | – | – | 21.44 ± 0.05 | – | 20.93 ± 0.03 | – |
| 57012.0 | 20141221 | 80.7 | 23.14 ± 0.20 | 23.34 ± 0.25 | 21.63 ± 0.05 | 23.34 ± 0.25 | 21.77 ± 0.07 | 23.34 ± 0.25 | 21.24 ± 0.05 | 23.34 ± 0.25 |
| 57014.0 | 20141223 | 82.6 | 22.67 ± 0.07 | 22.76 ± 0.12 | 21.71 ± 0.03 | 22.76 ± 0.12 | 21.79 ± 0.04 | 22.76 ± 0.12 | 21.29 ± 0.03 | 22.76 ± 0.12 |
| 57019.1 | 20141228 | 87.5 | 22.93 ± 0.16 | 23.05 ± 0.22 | 21.84 ± 0.06 | 23.05 ± 0.22 | 22.07 ± 0.07 | 23.05 ± 0.22 | 21.54 ± 0.07 | 23.05 ± 0.22 |
| 57026.1 | 20150104 | 94.2 | 23.12 ± 0.32 | 23.15 ± 0.39 | 22.21 ± 0.11 | 23.15 ± 0.39 | 22.36 ± 0.11 | 23.15 ± 0.39 | 21.90 ± 0.07 | 23.15 ± 0.39 |
| 57033.0 | 20150111 | 100.8 | 23.80 ± 0.29 | 23.98 ± 0.33 | 22.40 ± 0.07 | 23.98 ± 0.33 | 22.76 ± 0.12 | 23.98 ± 0.33 | 22.17 ± 0.08 | 23.98 ± 0.33 |
| 57040.0 | 20150118 | 107.5 | 23.42 ± 0.21 | 23.39 ± 0.24 | 22.76 ± 0.09 | 23.39 ± 0.24 | 22.90 ± 0.12 | 23.39 ± 0.24 | 22.34 ± 0.09 | 23.39 ± 0.24 |
| 57045.1 | 20150123 | 112.3 | 24.22 ± 0.39 | 24.32 ± 0.42 | 22.89 ± 0.13 | 24.32 ± 0.42 | 23.19 ± 0.26 | 24.32 ± 0.42 | 22.92 ± 0.26 | 24.32 ± 0.42 |
| 57052.1 | 20150130 | 119.0 | 23.77 ± 0.46 | 23.68 ± 0.49 | 23.58 ± 0.34 | 23.68 ± 0.49 | 23.78 ± 0.34 | 23.68 ± 0.49 | 22.86 ± 0.15 | 23.68 ± 0.49 |

*Notes.* Note that this observer-frame photometry has not been corrected for Milky Way extinction and quoted uncertainties are purely statistical. For our analysis, these have been added in quadrature with an error of 0.05 mag to represent systematic uncertainty, and these are included in the rest-frame photometry. Phases are given with respect to explosion.
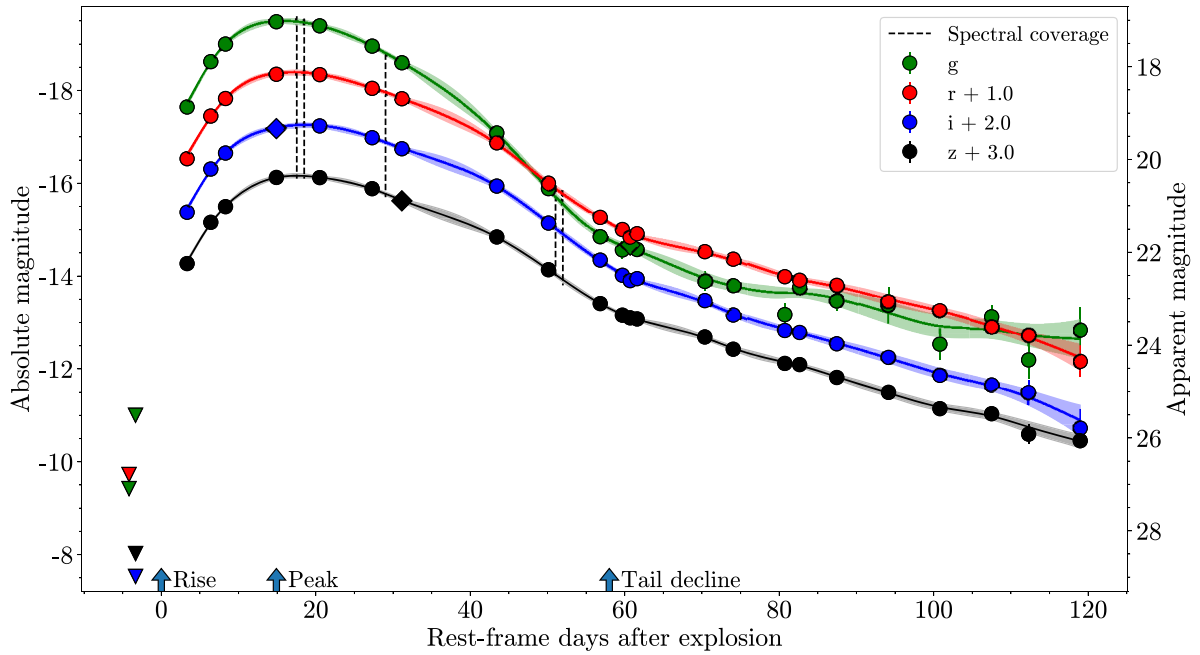


**Figure 1.** *griz* light curves of DES14X2fna, corrected for Milky Way extinction and *k*-corrected to the rest frame. Missing epochs of data have been interpolated using GP-interpolation. The dashed vertical lines indicate the epochs of spectral coverage, and the triangles prior to explosion denote upper limits. Diamond markers for data points indicate that they were reconstructed based on GP-interpolation of the full observer-frame light curve.

across the full light curve with minimal unphysical undulations. This error is reflected in the rest-frame photometry in Table 1. The GP-interpolated light curve used to reconstruct missing data was applied in the observer-frame – as such, it is not plotted with the rest-frame data in this figure. Instead, the GP-interpolation shown is obtained from this rest-frame data and is included to illustrate fits obtained from GP-interpolation. The length-scale of the GP fit was determined by maximizing the likelihood of the interpolation.

Spectroscopy of DES14X2fna was taken between +17.5 and + 52 d (all phases stated in this paper are in the rest frame and with respect to explosion epoch). These spectra were obtained with three different instruments: the AAOmega spectrograph at the Anglo-Australian Telescope (AAT) as part of the OzDES spectroscopic follow-up program, the Kast Double Spectrograph at Lick Observatory (LO), and the Blue Channel Spectrograph at the MMT Observatory. Details of the spectroscopic observations are in Table 2.

**Table 2.** Details of spectroscopy available for DES14X2fna.

| UT date | MJD | Rest-frame phase (d) | Telescope + instrument | Range (Å) |
|---|---|---|---|---|
| 20141016 | 56946 | + 17.5 | MMT + BCS | 3340–8550 |
| 20141017 | 56947 | + 18.5 | LICK + Kast | 3400–10 000 |
| 20141028 | 56958 | + 29 | AAT + 2dF/AAOmega | 3740–8950 |
| 20141120 | 56981 | + 51 | AAT + 2dF/AAOmega | 3740–8940 |
| 20141121 | 56982 | + 52 | AAT + 2dF/AAOmega | 3740–8950 |

*Notes.* BCS – Blue Channel Spectrograph on MMT 6.5-m telescope;
Kast – Kast Double Spectrograph on the 3m Shane telescope at Lick Observatory;
2dF/AAOmega – 2dF fibre positioner and AAOmega spectrograph on the 3.9-m AAT.
Phases are given with respect to explosion.
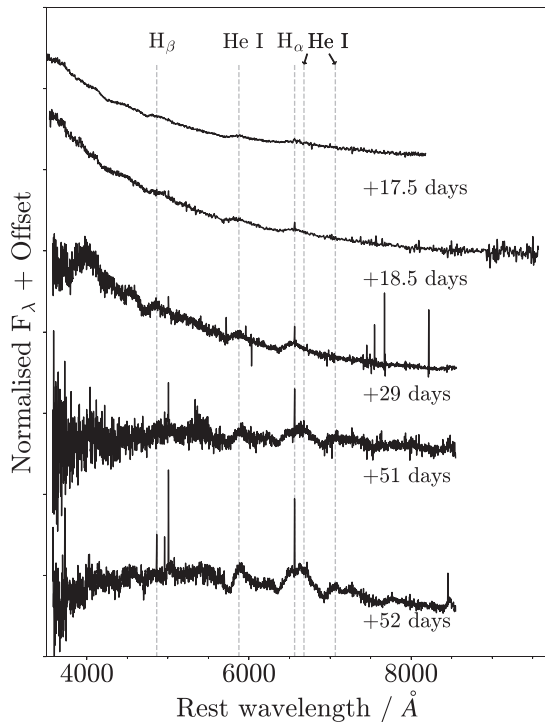


**Figure 2.** Optical spectra of DES14X2fna. Each spectrum has been smoothed using a Savitzky–Golay filter. Spectra have been offset by an arbitrary amount for clarity, and corrected for redshift and Milky Way reddening using the extinction model of Fitzpatrick & Massa (2007).

Spectroscopic reductions were performed using standard procedures; the AAT spectrum was reduced following the procedure outlined in Childress et al. (2017).

The spectral evolution of DES14X2fna is shown in Fig. 2. Note that as these spectra are only used for classification and calculating line velocities, they have not been calibrated to match photometry. Based on the presence of hydrogen at 18.5 d, it was initially classified as an SN II (Graham et al. 2014). The appearance of helium at 52 d led to a reclassification as an SN IIb (Kuehn et al. 2014).

# 3 CHARACTERIZING DES14X2FNA

## 3.1 Host galaxy

DES14X2fna was located in an anonymous host galaxy at a redshift of 0.0453. Assuming peculiar velocity dispersion of 200 km s$^{-1}$, this corresponds in our assumed cosmology to a distance of
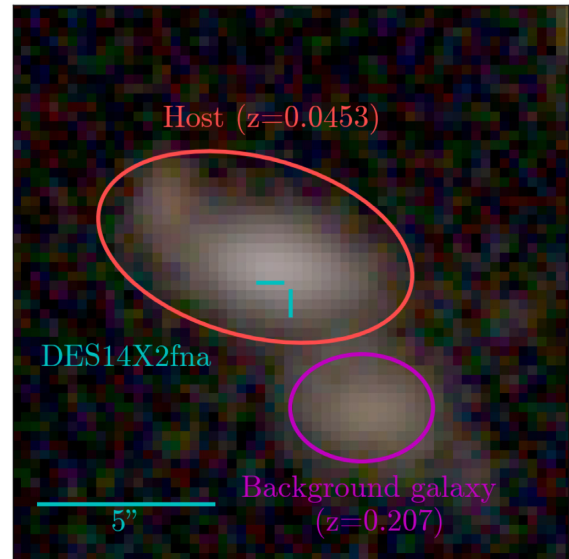


**Figure 3.** A composite *gri*-band image of the host galaxy of DES14X2fna, from the stacked templates of the DES-SN field of Wiseman et al. (2020a). The location of the SN is indicated by the blue markers. The adjacent galaxy, shown by the purple circle, is at higher redshift and not in proximity to the host.

200.7 ± 3.0 Mpc or a distance modulus of $\mu = 36.51 \pm 0.03$ mag. To infer global properties of the host, we use *griz*-band photometry from the deep stacked templates of the DES-SN fields described in Wiseman et al. (2020a). A composite *gri*-band image of the host galaxy from these templates is shown in Fig. 3. The neighbouring galaxy is at $z = 0.207$. This photometry corresponds to an absolute magnitude of $M_r = -16.35 \pm 0.03$. To estimate the stellar mass ($M_{\mathrm{stellar}}$) and SFR, we fit stellar population synthesis models based on the templates of Bruzual & Charlot (2003) with a Chabrier (2003) initial mass function (IMF), as per Wiseman et al. (2020b). We measure $\log_{10}(M_*/M_\odot) = 8.13^{+0.16}_{-0.07}$ and $\log_{10}(\mathrm{SFR}/M_\odot\,\mathrm{yr}^{-1}) = -1.53^{+0.23}_{-0.47}$. We find consistent results when fitting with PÉGASE.2 templates and a Kroupa IMF using the method of Smith et al. (2020).

We also derive abundance measurements from nebular emission lines in the host galaxy spectrum[2] from the OzDES survey (Lidman et al. 2020), a spectroscopic redshift follow-up programme for DES. Emission-line measurements and abundance calculations are performed using the method outlined in Wiseman et al. (2020b).

---

[2]Host spectrum of the host of DES14X2fna was taken in 2018 September, by which time the SN had completely faded from view.

**Table 3.** Properties of the host galaxy of DES14X2fna.

| Property | Host value |
|---|---|
| $M_g$ | $-16.01 \pm 0.04$ mag |
| $M_r$ | $-16.34 \pm 0.04$ mag |
| $M_i$ | $-16.50 \pm 0.05$ mag |
| $M_z$ | $-16.56 \pm 0.05$ mag |
| Redshift | $0.0453 \pm 0.0005$ |
| $E(B-V)_{MW}$ | $0.0225$ mag |
| $\log_{10}(M_*/M_\odot)$ | $8.13^{+0.16}_{-0.07}$ |
| $\log_{10}(SFR/M_\odot yr^{-1})$ | $-1.53^{+0.26}_{-0.48}$ |
| $\log_{10}(sSFR/yr^{-1})$ | $-9.66^{+0.10}_{-0.41}$ |
| Metallicity: S2N2 D16 | $7.76^{+0.31}_{-0.54}$ dex |
| Metallicity: PP04 N2 | $8.17^{+0.11}_{-0.17}$ dex |
| Metallicity: PP04 O3N2 | $8.19^{+0.09}_{-0.14}$ dex |
| Metallicity: KK04 R23 | $8.17^{+0.20}_{-0.23}$ dex |

Briefly, we subtract the stellar continuum as well as any Balmer line absorption using the Penalized PiXel-Fitting software (PPXF; Cappellari & Emsellem 2004; Cappellari et al. 2012; Cappellari 2017) with the MILES library of single stellar populations (Vazdekis et al. 2010), and fit the resulting gas spectrum with Gaussian profiles. We use the line fluxes to derive metallicities based on a number of different calibrations: S2N2 (Dopita et al. 2016), N2 and O3N2 (Pettini & Pagel 2004), and R23 (Kewley, Geller & Jansen 2004) (Table 3).

Comparing our calculated mass of the host of DES14X2fna with previous studies of stellar masses of core-collapse SN hosts (e.g. fig. 4 of Galbany et al. 2018; fig. 11 of Wiseman et al. 2020a; fig. 14 of Schulze et al. 2020) indicates that this is a relatively low-mass host, although not unusually low for an SN IIb. The PISCO sample of host galaxies presented in Galbany et al. (2018) contains 13 SNe IIb host environments – this sample varies in PP04 O3N2 metallicity between approximately 8.4 and 8.7 and in $\log_{10}(sSFR/yr^{-1})$ between approximately $-11.2$ and $-9.5$. DES14X2fna is lower metallicity than any of these hosts but falls in the upper end of the distribution in terms of sSFR. The PTF sample presented in Schulze et al. (2020) contains 61 SNe IIb hosts that extend down to $10^6$ $M_\odot$. For this sample, $\log_{10}(sSFR/yr^{-1})$ varies from approximately $-12$ to $-8$. The host of DES14X2fna sits towards the upper end of this distribution although it is not as standout as compared to the PISCO sample.

In summary, the host of DES14X2fna is a low-mass, low-metallicity but relatively highly star-forming galaxy. The majority of core-collapse SNe are observed across a wide range of star-forming hosts (Anderson et al. 2010). However, the most energetic form of stripped envelope SN, SNe Ic-BL, are observed preferentially in low-mass, low-metallicity, star-forming environments similar to DES14X2fna (Japelj et al. 2018; Modjaz et al. 2020).

### 3.2 Photometry

The rest-frame *griz* light curves of DES14X2fna are shown in Fig. 1. After explosion, DES14X2fna rises to a peak *g*-band absolute magnitude of $\simeq -19.5$, and $\simeq -19.3$, $\simeq -19.2$, and $\simeq -19.1$ in *riz* bands, respectively. After peak, the *g* band declines by $\sim 5$ mag in $\sim 40$ d, while *riz* decline by $\sim 3$ mag over the same period. After approximately 60 d, each band appears to show a roughly linear decline. GP-interpolation can be used to estimate the rise time and peak absolute magnitude, but does not directly provide us with

**Table 4.** Peak absolute magnitudes of DES14X2fna estimated from GP interpolation.

| Filter | Peak absolute magnitude (mag) | Rise time (d) |
|---|---|---|
| $g$ | $-19.47 \pm 0.06$ | $16.67 \pm 0.53_{stat} \pm 3.35_{sys}$ |
| $r$ | $-19.37 \pm 0.05$ | $18.00 \pm 0.56_{stat} \pm 3.35_{sys}$ |
| $i$ | $-19.23 \pm 0.06$ | $18.90 \pm 0.58_{stat} \pm 3.35_{sys}$ |
| $z$ | $-19.14 \pm 0.05$ | $18.35 \pm 0.57_{stat} \pm 3.35_{sys}$ |

*Note.* Statistical errors in rise time estimated from MC approach, systematic errors correspond to uncertainty in explosion epoch between last non-detection and first detection in rest frame.

uncertainties on rise time. We estimate these using a Monte Carlo approach, randomizing the rest-frame photometry within error bars and GP-interpolating this to estimate the rise time and peak absolute magnitude. This is repeated 1000 times, with the mean and standard deviation taken as the final values and uncertainties. These values are shown in Table 4.

To characterize the light curve of DES14X2fna relative to the population of SNe IIb, we have gathered a comparison sample of spectroscopically confirmed SNe IIb. We have selected objects with publicly-available photometry with good coverage around peak and a well-constrained explosion epoch, either through light-curve modelling or a short period between last non-detection and first detection (15 d is the maximum in our sample). This leaves us with a sample of 22 SNe IIb (see Table 5).

The top panel of Fig. 4 shows the rest-frame *r*-band light curve of DES14X2fna along with *r*/*R*-band light curves of our SNe comparison sample. Note that SN 2009mg, SN 2011ei and SN 2013cu lack sufficient *r*/*R*-band coverage and so we have used *V*-band photometry as the closest wavelength band available to *R*. For each object we use GP-interpolation to estimate the rise time and peak absolute magnitude. We estimate the epoch at which the linear decline phase of the light curve begins for each SN, $t_{tail}$ and the absolute magnitude at this epoch, $M_{tail}$, by eye, where these could be inferred from the data. In addition, we perform linear fits to calculate the tail decline rate where possible. Details and parameter values of each SN in our comparison sample are given in Table 5. We have corrected the light curves for redshift and Milky Way extinction based on values reported in the respective papers outlined in this table. However, as these objects are all at low redshift, we do not K-correct these light curves to the rest frame since the effect will be small. Uncertainties in quoted peak absolute magnitude ($M_{peak, MW}$) incorporate uncertainty in GP-interpolation to observed photometry and Milky Way extinction correction. Distances are estimated by cross-matching SNe with their hosts using the NASA Extragalactic Database (NED[3]) and obtaining a luminosity distance in our assumed cosmology corrected for Virgo infall. We choose this approach for consistency as some of these hosts do not have redshift-independent distance estimates and where they do these are often calculated for different cosmologies. The exception to this is SN 1993J, as the negative redshift of the host means that a redshift distance is not appropriate – instead, we adopt the literature value of $2.9 \pm 0.4$ Mpc from Lennarz, Altmann & Wiebusch (2012). Distance uncertainties are included in this analysis. Where data are available, we correct

---

[3] The NASA/IPAC Extragalactic Database (NED) is operated by the Jet Propulsion Laboratory, California Institute of Technology, under contract with the National Aeronautics and Space Administration (http://ned.ipac.caltech.edu)

**Table 5.** Details and light-curve properties of our SN IIb comparison sample.

| SN | Redshift | $E(B-V)_{MW}$ (mag) | $E(B-V)_{host}$ (mag) | Rise time (d) | $M_{peak, MW}$ (mag) | $M_{peak, host}$ (mag) | $t_{tail}$ (d) | $M_{tail}$ (mag) | Tail decline rate (mag 100 d$^{-1}$) | References |
|---|---|---|---|---|---|---|---|---|---|---|
| DES14X2fna | 0.0453 | $0.0225 \pm 0.0003$ | Negligible | $18.00 \pm 0.56_{stat} \pm 3.35_{sys}$ | $-19.37 \pm 0.05$ | – | 60 | $-16$ | $4.30 \pm 0.10$ | – |
| ASASSN-18am | 0.0301 | $0.0086 \pm 0.0011$ | Negligible | $18.89 \pm 0.42_{stat} \pm 0.39_{sys}$ | $-19.53 \pm 0.04$ | – | 60 | $-17.3$ | $3.03 \pm 0.06$ | (1) |
| SN 2016gkg | 0.0049 | $0.0166 \pm 0.0002$ | $0.09^{+0.08}_{-0.07}$ | $20.39 \pm 1.11_{stat} \pm 0.16_{sys}$ | $-16.69 \pm 0.06$ | $-16.97^{+0.26}_{-0.22}$ | 43 | $-16$ | $1.63 \pm 0.08$ | (2), (3), (4), (5), (6), (7) |
| SN 2013cu$^a$ | 0.0252 | $0.0105 \pm 0.0003$ | N/A | $9.79 \pm 1.08_{stat} \pm 0.97_{sys}$ | $-18.51 \pm 0.07$ | – | – | – | – | (2), (8) |
| SN 2013df | 0.0024 | $0.0168 \pm 0.0002$ | $0.081 \pm 0.016$ | $22.32 \pm 0.68_{stat}$ | $-15.54 \pm 0.04$ | $-15.80 \pm 0.06$ | 40 | $-14.8$ | $1.96 \pm 0.02$ | (2), (9), (10), (11), (12) |
| SN 2012P | 0.0045 | $0.0437 \pm 0.0005$ | $0.29^{+0.08}_{-0.05}$ | $20.32 \pm 0.19_{stat}$ | $-15.93 \pm 0.03$ | $-16.83^{+0.25}_{-0.16}$ | [50,60] | [$-14, -14.2$] | $1.44 \pm 0.02$ | (2), (13) |
| SN 2011dh | 0.0016 | $0.0309 \pm 0.0017$ | <0.05 | $21.89 \pm 0.19_{stat} \pm 0.88_{sys}$ | $-17.47 \pm 0.03$ | – | 48 | $-15.8$ | $2.02 \pm 0.03$ | (2), (9), (14), (15), (16) |
| SN 2011ei$^a$ | 0.0093 | $0.0505 \pm 0.0008$ | 0.18 | $11.84 \pm 0.70_{stat}$ | $-16.14 \pm 0.07$ | $-16.70 \pm 0.07$ | – | – | – | (2), (17) |
| SN 2011fu | 0.0185 | $0.0648 \pm 0.0008$ | $0.15 \pm 0.11$ | $20.47 \pm 0.54_{stat}$ | $-18.01 \pm 0.03$ | $-18.48 \pm 0.34$ | [40,45] | [$-17.2, -17.4$] | $1.69 \pm 0.05$ | (18), (19) |
| SN 2011hs | 0.0057 | $0.0104 \pm 0.0004$ | $0.16 \pm 0.07$ | $17.91 \pm 0.29_{stat}$ | $-16.35 \pm 0.03$ | $-16.85 \pm 0.22$ | 35 | $-15.1$ | $2.14 \pm 0.02$ | (2), (20) |
| SN 2009K | 0.0117 | $0.0491 \pm 0.0014$ | N/A | $27.46 \pm 0.41_{stat} \pm 1.21_{sys}$ | $-17.61 \pm 0.03$ | – | – | – | – | (21), (22), (23), (24) |
| SN 2009mg$^a$ | 0.0076 | $0.0388 \pm 0.0005$ | $0.09 \pm 0.02$ | $21.06 \pm 1.00_{stat}$ | $-16.70 \pm 0.05$ | $-16.98 \pm 0.08$ | – | – | – | (2), (25) |
| SN 2008aq | 0.008 | $0.0386 \pm 0.0009$ | 0.027 | $20.11 \pm 0.44_{stat}$ | $-16.91 \pm 0.04$ | $-17.00 \pm 0.04$ | 47 | $-15.7$ | $2.18 \pm 0.04$ | (2), (21), (22), (26) |
| SN 2008ax | 0.0019 | $0.0188 \pm 0.0002$ | $0.38 \pm 0.1$ | $23.92 \pm 1.07_{stat}$ | $-16.32 \pm 0.04$ | $-17.50 \pm 0.31$ | 40 | $-15.3$ | $2.13 \pm 0.03$ | (2), (22), (27), (28) |
| SN 2006el | 0.017 | $0.0975 \pm 0.0012$ | N/A | $22.21 \pm 1.00_{stat}$ | $-17.14 \pm 0.09$ | – | – | – | – | (22), (29) |
| SN 2006T | 0.0081 | $0.0643 \pm 0.0007$ | N/A | $22.83 \pm 0.23_{stat} \pm 7.63_{sys}$ | $-17.15 \pm 0.03$ | – | 48 | $-15.9$ | $1.79 \pm 0.02$ | (2), (21), (22) |
| SN 2004ex | 0.018 | $0.0184 \pm 0.0016$ | N/A | $25.67 \pm 0.56_{stat} \pm 10.43_{sys}$ | $-17.10 \pm 0.03$ | – | 54 | $-15.9$ | $2.06 \pm 0.08$ | (22) |
| SN 2004ff | 0.023 | $0.0274 \pm 0.001$ | N/A | $11.82 \pm 0.37_{stat}$ | $-17.27 \pm 0.03$ | – | 40 | $-16$ | $1.88 \pm 0.08$ | (21), (29), (30) |
| SN 2003bg | 0.0046 | $0.018 \pm 0.001$ | Negligible | $49.41 \pm 0.81_{stat}$ | $-16.36 \pm 0.04$ | – | – | – | $1.29 \pm 0.06$ | (31) |
| SN 2001ig | 0.0031 | $0.0089 \pm 0.0004$ | <0.09 | $30.14 \pm 3.86_{stat}$ | $-18.01 \pm 0.07$ | – | – | – | – | (32) |
| SN 1996cb | 0.0024 | $0.0261 \pm 0.0005$ | <0.12 | $24.09 \pm 0.67_{stat}$ | $-16.10 \pm 0.05$ | – | 44 | $-15.6$ | $2.21 \pm 0.03$ | (33) |
| SN 1993J | $-0.0001$ | $0.069 \pm 0.0001$ | $0.12 \pm 0.07$ | $20.99 \pm 4.42_{stat}$ | $-15.75 \pm 0.04$ | $-16.12 \pm 0.22$ | 40 | $-14.7$ | $2.18 \pm 0.02$ | (9), (34), (35), (36), (37), (38), (39), (40), (41), (42), (43) |

*References.* (1) Bose et al. (2020); (2) Brown et al. (2014); (3) Bersten et al. (2018); (4) Tonry et al. (2016); (5) Arcavi et al. (2017b); (6) Nicholls et al. (2016); (7) Kilpatrick et al. (2016); (8) Ofek et al. (2014); (9) Tinyanont et al. (2016); (10) Szalai et al. (2016); (11) Maeda et al. (2015); (12) Morales-Garoffolo et al. (2014); (13) Fremling et al. (2016); (14) Ergon et al. (2015); (15) Sahu, Anupama & Chakradhari (2013); (16) Helou et al. (2013); (17) Drake et al. (2009); (18) Kumar et al. (2013); (19) Ciabattari & Mazzoni (2011); (20) Bufano et al. (2014); (21) Stritzinger et al. (2018); (22) Bianco et al. (2014); (23) Hicken et al. (2017); (24) Pignata et al. (2009); (25) Monard (2009); (26) Chu et al. (2008); (27) Tsvetkov et al. (2009); (28) Pastorello et al. (2008); (29) Drout et al. (2011); (30) Pugh, Park & Li (2004); (31) Galbany et al. (2016); (32) Kato et al. (2004); (33) Qiu et al. (1999); (34) Richmond et al. (1996); (35) Barbon et al. (1995); (36) Metlova et al. (1995); (37) Richmond et al. (1994); (38) Lewis et al. (1994); (39) Benson et al. (1994); (40) van Driel et al. (1993); (41) Okyudo et al. (1993); (42) Mikuz, Dintinjana & Zwitter (1993); (43) Zhou (1993). Missing host extinction values have been labelled as either negligible based on spectroscopy or N/A if no host extinction data was available. All presented magnitudes are in AB system. Where SN explosion dates were calculated using the dates of first detection and last non-detection, rise time uncertainties have quoted systematic errors as in Table 4. These values are not quoted where explosion epochs were sourced from literature using other methods. $^a$These properties were calculated using $r/R$-band photometry with the exception of SNe, for which $V$-band light curves were used due to a lack of $r/R$-band data.

for host extinction and factor this into the peak absolute magnitude $M_{peak, host}$. However, as these data were not available for all objects and only an upper limit, in some cases, we do not correct for host extinction when considering bolometric luminosities in order to be consistent across all objects.

The most noticeable feature of DES14X2fna is its very high peak luminosity, 0.2 mag fainter than the very luminous ASASSN-18am at peak but nearly one mag brighter than the next brightest object in the sample, SN 2013cu. It is important to note that host extinction can make a significant difference to the luminosity of each object, as in the case of SN 2008ax that shows an increase in peak luminosity of greater than 1 mag. However, as most objects have a host extinction considerably less than this and DES14X2fna is significantly more luminous than most of the sample, DES14X2fna still stands out for its considerable luminosity even when accounting for this possibility. DES14X2fna rises to peak in the *r* band in 18 d, similar to ASASSN-18am and SN 2011hs and fairly typical for SNe IIb based on the sample of SN IIb rise times presented in fig. 4 of Pessi et al. (2019). After rising to maximum, DES14X2fna declines at a similar rate to ASASSN-18am until ∼30 d after explosion, after which DES14X2fna begins to decline far more rapidly.

DES14X2fna has a single-peaked light curve similar to SN 2008ax and unlike the well-studied SN 1993J. However, as there is a period of ≃7 d between the last non-detection and first detection it is possible that an initial peak did occur but was not observed, as this has been observed to last only a few days in previous SNe (Okyudo et al. 1993; Helou et al. 2013; Tartaglia et al. 2017).

Motivated by the bright peak luminosity of DES14X2fna, we also compare to SNe Ic-BL to study any resemblance to this very energetic class of stripped-envelope SNe. Following the method for our SN IIb sample, we form a similar comparison sample of SNe Ic-BL (Table 6), and light curves shown in the lower panel of Fig. 4. Overall, the peak of DES14X2fna resembles that of an SN Ic-BL more closely than a typical SN IIb. Most notably, in the *r* band, DES14X2fna matches SN 1998bw well until ≃30 d after explosion. After this time DES14X2fna declines more rapidly than SN 1998bw.

As is evident from both panels of Fig. 4, after peak, DES14X2fna exhibits a very rapid tail decline compared to both SNe IIb and SNe Ic-BL. The top panel of Fig. 5 focuses on this decline phase for each SN in our SN IIb comparison sample where a tail is apparent. For each SN in the plot, we fit a line to the tail to estimate the decline rate (Table 5). DES14X2fna has an *r*-band decline rate of $4.30 \pm 0.10$ mag $(100 \, d)^{-1}$, significantly faster than ASASSN-18am, the next fastest decliner in the sample $(3.03 \pm 0.06$ mag $(100 \, d)^{-1})$. The lower panel of Fig. 5 also shows a histogram of the estimated decline rates for our sample, where DES14X2fna is a clear outlier.

It is clear that DES14X2fna exhibits both a very luminous peak and a faster tail evolution than other previously observed SNe IIb. If we are to assume that this object follows the canonical $^{56}$Ni decay model for an SN IIb, high $^{56}$Ni and ejecta masses would be required to power the high maximum luminosity and broad peak
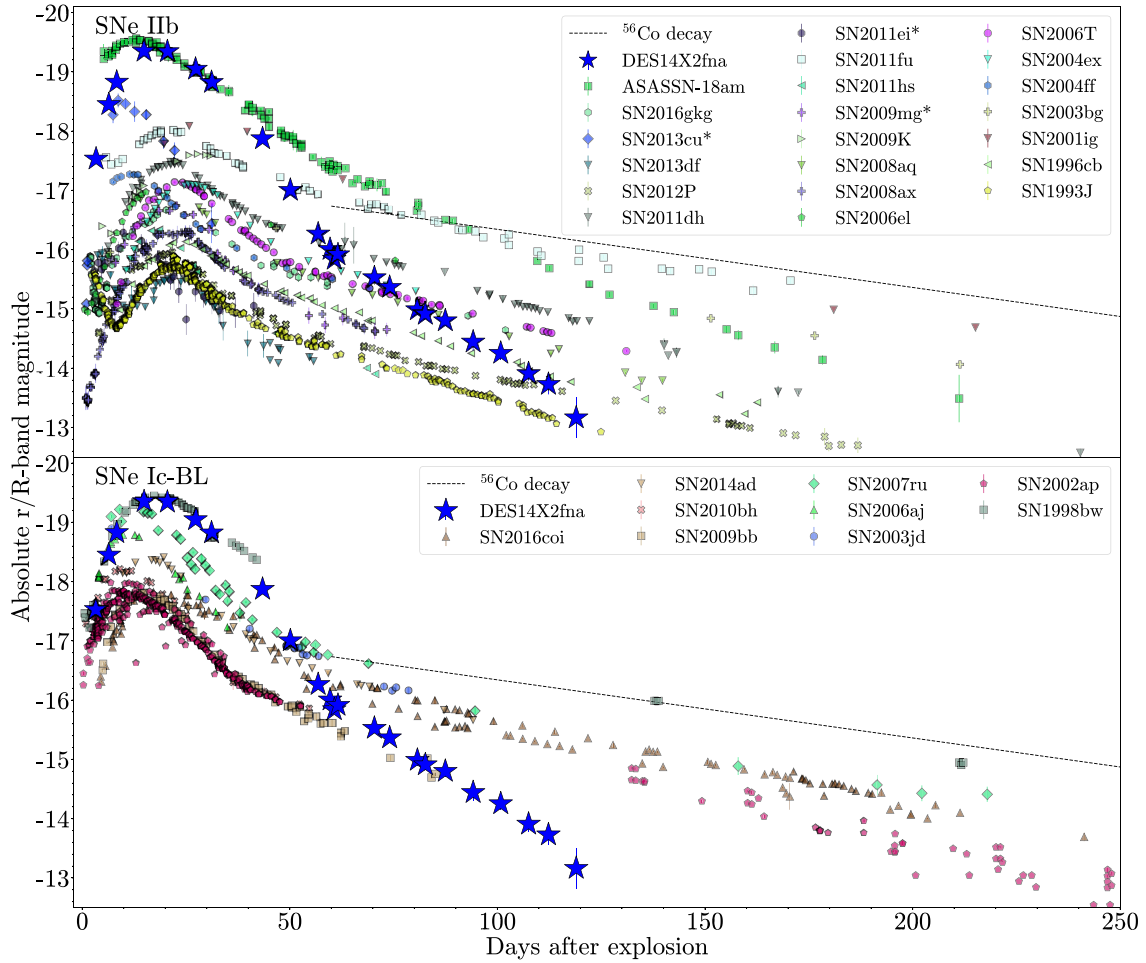
**Figure 4.** Upper panel: *r*-band light curve of DES14X2fna alongside the *r/R*-band light curves of our SN IIb comparison sample. The dashed line indicates the decline rate expected for fully trapped $^{56}$Co decay. Objects denoted with ∗ in the legend show *V*-band photometry due to a lack of available *r/R*-band data. Lower panel: same as upper panel but for a comparison sample of SNe Ic-BL. All light curves are corrected for MW extinction, and DES14X2fna is *k*-corrected to the rest frame.

**Table 6.** Our SN Ic-BL comparison sample.

| SN | Redshift | $E(B-V)_{MW}$ | References |
|---|---|---|---|
| SN 2016coi | 0.003 646 | 0.0737 | (1) |
| SN 2014ad | 0.0057 | 0.038 | (2) |
| SN 2010bh | 0.0593 | 0.1004 | (3) |
| SN 2009bb | 0.0104 | 0.0847 | (4), (5) |
| SN 2007ru | 0.0155 | 0.2217 | (6), (7) |
| SN 2006aj | 0.033 023 | 0.1261 | (6) |
| SN 2003jd | 0.019 | 0.0378 | (6) |
| SN 2002ap | 0.002 108 | 0.0616 | (6), (8), (9), (10), (11) |
| SN 1998bw | 0.0085 | 0.0494 | (12), (13), (14), (15) |

*Referenes.* (1) Prentice et al. (2018); (2) Sahu et al. (2018); (3) Cano et al. (2011); (4) Stritzinger et al. (2018); (5) Pignata et al. (2011); (6) Bianco et al. (2014); (7) Sahu et al. (2009); (8) Foley et al. (2003); (9) Yoshii et al. (2003); (10) Pandey et al. (2003); (11) Gal-Yam, Ofek & Shemmer (2002); (12) Sollerman et al. (2002); (13) Patat et al. (2001); (14) Sollerman et al. (2000); (15) Galama et al. (1998).

of DES14X2fna. However, a high ejecta mass would be expected to lead to complete trapping of the γ-rays produced in $^{56}$Co decay at late times as there would be significant surrounding material to absorb these γ-rays. Not only does DES14X2fna decline at a rate far faster

than expected for fully trapped $^{56}$Co decay, it declines more than 1.0 mag $(100\,\mathrm{d})^{-1}$ faster than any other SN IIb in our comparison sample. This raises the question as to whether the light curve of DES14X2fna is consistent with a $^{56}$Ni decay model or if an alternative mechanism to power the light curve is required.

### 3.3 Bolometric luminosity

We next consider the bolometric and pseudo-bolometric light curves of DES14X2fna. Observed *griz* light curves are converted to luminosities by fitting with a blackbody curve to compute a spectral energy distribution (SED). The exact values and uncertainties in bolometric luminosities were estimated using a Monte Carlo approach:

(i) An initial blackbody fit is carried out to estimate photospheric radius and temperature along with their uncertainties.

(ii) Randomized radius and temperature values are then drawn from a Gaussian distribution using the best-fitting values and uncertainties and used to generate a randomized blackbody SED.

(iii) Each randomized SED is integrated over the wavelength range covered by *griz* bands to produce a pseudo-bolometric luminosity, $L_{griz}$. A bolometric luminosity $L_{bol}$ is estimated by integrating the fitted SED over all wavelengths.
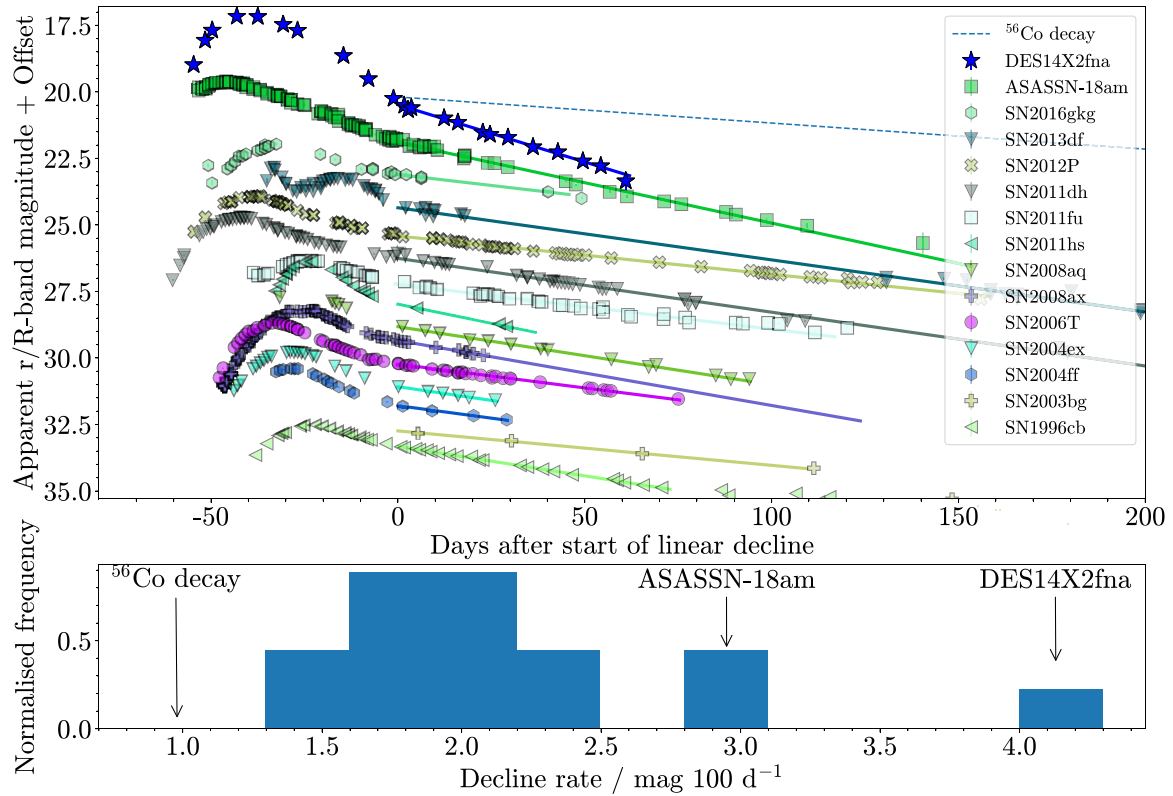
**Figure 5.** Upper panel: *r*-band light curve of DES14X2fna and the *r/R*-band light curves of the SNe in the SN IIb comparison sample that exhibit a linear decline. The solid lines show a linear fit to the post-peak linear decline of each SN. Lower panel: histogram showing *r/R*-band decline rates estimated from the linear fits in upper panel, with DES14X2fna annotated.

(iv) This process is then repeated, with the final values of $L_{griz}$ and $L_{bol}$ as well as their uncertainties calculated from the mean and standard deviation of values from all of the randomized blackbody SEDs.

We also considered estimating bolometric luminosity using our mangled SED models and the bolometric corrections outlined in Lyman, Bersier & James (2013), but find that these obtain consistent results with our blackbody approach. As a result, we use blackbody fits since these provide information on photospheric temperature and radius as well as luminosity. Of course, the blackbody approximation is not valid at later times as the SN enters the nebular phase; hence, we do not estimate bolometric luminosity more than 120 d after explosion, after our last observation of DES14X2fna. At later times the decreasing quality of a blackbody fit is reflected in larger fit uncertainties and hence much larger uncertainties in $L_{bol}$ and $L_{griz}$. In addition to this, further uncertainty in $L_{bol}$ arises from the lack of flux information beyond optical wavelengths, particularly in the UV. Without observations at these wavelengths, we are not able to quantify this effect but acknowledge that it will serve to increase our uncertainties.

To calculate bolometric light curves for our SNe IIb comparison sample, we make cuts to select only SNe with observations in at least three photometric bands around peak luminosity to allow reasonable blackbody fits. Unlike DES14X2fna, our sample of SNe IIb includes objects with photometric data at very different epochs and phases of the light curve, which restricts the epochs at which we can calculate bolometric luminosities. At each epoch with available photometry, other observed bands were GP-interpolated to provide simultaneous photometry, after which the same procedure

outlined for DES14X2fna was carried out to estimate blackbody fit parameters and bolometric luminosities. To ensure consistency with our estimates of the pseudo-bolometric luminosity of DES14X2fna, we use the same wavelengths limits in our integration regardless of which photometric bands were available for each SN. The bolometric luminosities, photospheric radii, and temperatures obtained from our blackbody fits are shown in Fig. 6.

As with the *r/R*-band photometric data, aside from ASASSN-18am DES14X2fna is the most luminous object in the SN IIb sample and has a relatively broad light-curve peak. We can estimate the true peak bolometric luminosity and rise time using GP-interpolation, which gives a peak luminosity of $L_{bol} = (2.44 \pm 0.41) \times 10^{43}$ and $L_{griz} = (1.17 \pm 0.08) \times 10^{43}$ erg s$^{-1}$, with a rise time to peak, $t_p$, of 15.38 d. With the exception of ASASSN-18am and SN 2013cu, DES14X2fna is brighter at peak than any other SN in the sample by more than a factor of 2. This reiterates our findings from broad-band photometry: DES14X2fna is very luminous at maximum, comparable only to ASASSN-18am, and has a relatively broad light-curve peak.

The photospheric radius of DES14X2fna shows an initial fast rise, reaching $(1.86 \pm 0.08) \times 10^{15}$ cm after 20.5 d, suggesting a photospheric velocity of $\sim$7900 km s$^{-1}$. The radius then remains roughly constant for $\sim$30 d, before slowly decreasing again. This radius evolution is fairly typical for an SN IIb, most closely resembling SN 2011dh and SN 2004ff. ASASSN-18am also shows a similar radius evolution to DES14X2fna at early times, although declines more slowly after peak.

DES14X2fna and ASASSN-18am both show a similar temperature evolution, rising to $\sim$12 000 K at peak after $\sim$8–9 d, before declining roughly linearly to $\sim$5000 K after $\sim$50 d and staying
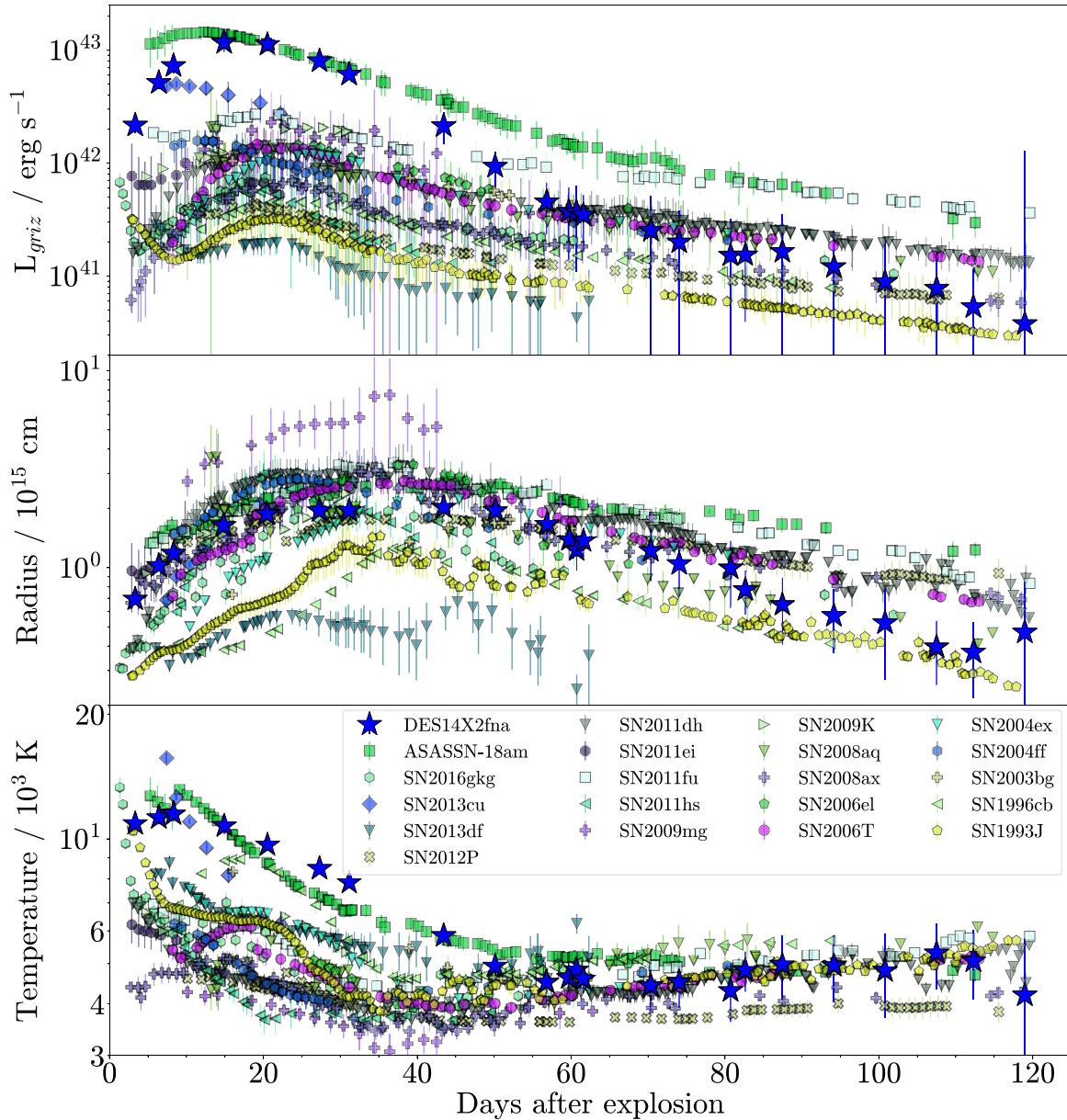
**Figure 6.** Upper panel: bolometric light curves of DES14X2fna and our SN IIb comparison sample, estimated from blackbody fits to observed photometry. Middle panel: photospheric radii for DES14X2fna and our SN IIb comparison sample estimated from blackbody fits. Lower panel: effective temperatures for DES14X2fna and our SN IIb comparison sample.

roughly constant thereafter, although ASASSN-18am declines more rapidly between ∼10 and 20 d. While SN 2016gkg and SN 2013cu do reach comparable temperatures, this occurs very soon after explosion due to shock cooling while DES14X2fna and ASASSN-18am show temperatures in excess of the rest of the SNe IIb sample until 50 d after explosion, with a far more prolonged temperature decline.

### 3.4 Spectroscopy

Spectroscopy of DES14X2fna is shown in Fig. 2. After ∼17.5 d, weak H β and He I 5876 lines become visible. Approximately one day later, a more noticeable broad H α feature is visible. From ∼29 d, the features become more prominent, with H α, H β, and He I 5876 all visible. These are still present in the later spectra at ∼50 d, albeit

with H β becoming increasingly noisy, and further He I features at 6678 and 7065 Å also appear in these later spectra.

Where possible, we have estimated the expansion velocities of these lines from their P-Cygni profiles, fitting a Gaussian with a pseudo-continuum to estimate the minimum and using this to infer velocity. We follow the process outlined in Maguire et al. (2012), fitting to a small wavelength range around each feature and considering a 30-Å range for the cutoff on either side of the feature when searching for the best fit. The velocity evolution of DES14X2fna is shown in Table 7.

Overall, H α and H β maintain a relatively constant velocity throughout all of our spectra of roughly 9000 km s$^{-1}$. He I 5876 has a velocity of 9254 ± 517 km s$^{-1}$ after 17.5 d, comparable to the H lines, before decreasing gradually in each spectrum and reaching 6074 ± 119 km s$^{-1}$ after 52 d. He I 7065 is not visible in the

**Table 7.** Expansion velocities of DES14X2fna at different phases calculated from position of minimum of P-Cygni profile.

| Line | Phase | $v_{exp}$ / km s$^{-1}$ |
|---|---|---|
| H $\alpha$ | + 29 | 8670 $\pm$ 660 |
| – | 51 | 8880 $\pm$ 740 |
| – | 52 | 9540 $\pm$ 510 |
| H $\beta$ | + 17.5 | 8250 $\pm$ 150 |
| – | 29 | 9110 $\pm$ 450 |
| – | 52 | 9620 $\pm$ 1830 |
| He I 5876 | + 17.5 | 9250 $\pm$ 520 |
| – | 29 | 8480 $\pm$ 300 |
| – | 51 | 6550 $\pm$ 970 |
| – | 52 | 6070 $\pm$ 490 |
| He I 7065 | + 51 | 6620 $\pm$ 770 |
| – | 52 | 6220 $\pm$ 490 |

early spectra but has velocities of 6616 $\pm$ 766 and 6219 $\pm$ 489 km s$^{-1}$ in the final two spectra, respectively, similar to He I 5876. The decreasing velocity of He but not H could result if almost all H present is located in the outer ejecta, meaning that there is little or no H below 8000–9000 km s$^{-1}$.

Fig. 7 shows a comparison of the spectra of DES14X2fna with the similarly luminous SN IIb ASASSN-18am and the 'prototypical' SN IIb SN 1993J. While DES14X2fna shows similar hydrogen and helium features to these objects, there are significant differences in the spectral evolution. Temperatures inferred from our blackbody fits in the lower panel of Fig. 6 show that DES14X2fna and ASASSN-18am are significantly hotter than SN 1993J until ∼50 d after explosion, and this is reflected in the continuum.

After ∼17.5 d, DES14X2fna and ASASSN-18am have only subtle features and are dominated by a blue continuum while SN 1993J has clear features. SN 1993J displays H $\alpha$ and He I 6678 lines that overlap to create a broader feature and an absorption feature appearing to correspond to H $\beta$, as well as He I 5876 features.

After 29 d, DES14X2fna is still hotter than SN 1993J and comparable to ASASSN-18am. DES14X2fna again appears very similar to ASASSN-18am with both showing a broad H $\alpha$ feature as well as H $\beta$ and He I 5876. For SN 1993J, at this epoch the broad feature at ∼6600 Å shows dips around the wavelength of H $\alpha$, indicating that the contribution of H to this broad feature has reduced. After 52 d, the H $\beta$ feature in DES14X2fna is no longer visible though may still be contained in the noise. However, H $\alpha$ is still visible and He I 6678 and 7065 lines are now apparent along with the He I 5876 line seen previously. ASASSN-18am lacks wavelength coverage above ∼6700 Å but still appears similar to DES14X2fna at this epoch, with H $\alpha$ and He I 5876 features as well as a noticeable H $\beta$ feature. At this epoch, SN 1993J continues the trend of a dip in the broad feature at ∼6600 Å around H $\alpha$, and now displays clear He I 7065 lines.

Overall, the spectral evolution of these objects shows that DES14X2fna maintains its H envelope for far longer than SN 1993J, with H features visible in the spectra of DES14X2fna at later epochs. This suggests that although the H envelope of the progenitor of DES14X2fna partially stripped, it still has a more massive H envelope than a typical SN IIb. This is also seen in ASASSN-18am, and Bose et al. (2020) discuss that this SN is also richer in H than other SNe IIb. Overall, DES14X2fna shows strong resemblance to ASASSN-18am over the epochs where we have spectroscopic coverage.
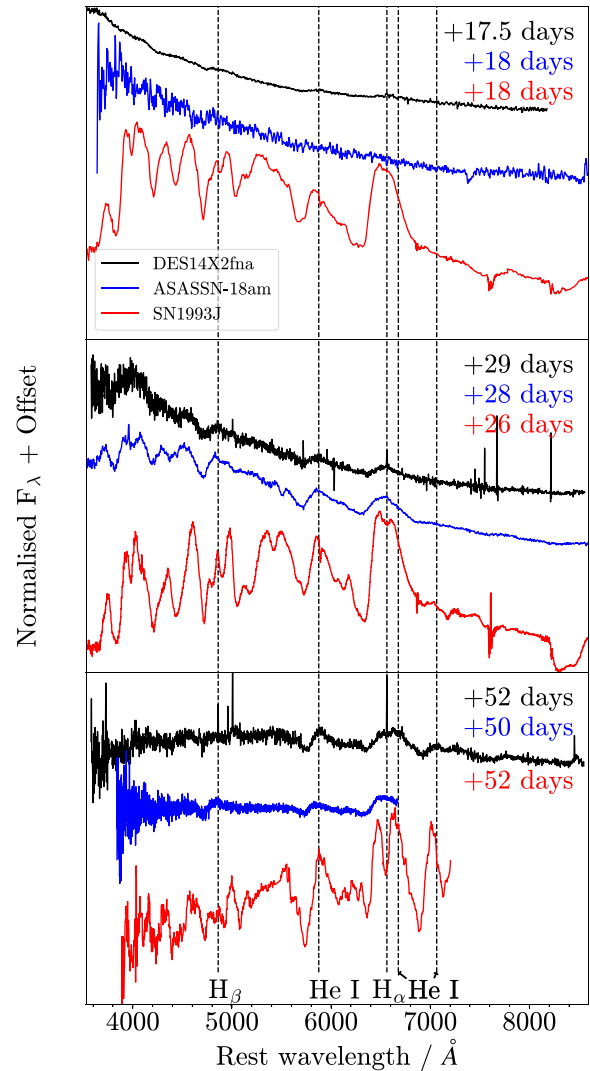


**Figure 7.** Spectroscopy of DES14X2fna between 17.5 and 52 d after explosion, alongside spectra of ASASSN-18am and SN 1993J. Spectra have been arbitrarily shifted for presentation and corrected for Milky Way reddening using the extinction model of Fitzpatrick & Massa (2007). Phases displayed in the top right-hand side are with respect to explosion.

## 4 SEMI-ANALYTIC LIGHT CURVE MODELLING

Our analysis has shown significant differences between DES14X2fna and previously observed SNe IIb, with regard to both its luminosity and fast decline rate. We next consider the possible sources of luminosity of DES14X2fna by making use of the fitting code MOSFIT (Guillochon et al. 2018). This uses a semi-analytic approach to light-curve fitting, combining models for different sources to drive luminosity in the system with others to model diffusion through the SN ejecta to produce an observed luminosity over time. From these, model photometric light curves can be generated by assuming a modified blackbody SED. Byfig8 using a Markov chain Monte Carlo (MCMC) approach to sample the parameter space for all of the models included, MOSFIT calculates the best-fitting light curve and parameters for a given model. We consider three different mechanisms included in MOSFIT to model the light curve of DES14X2fna:
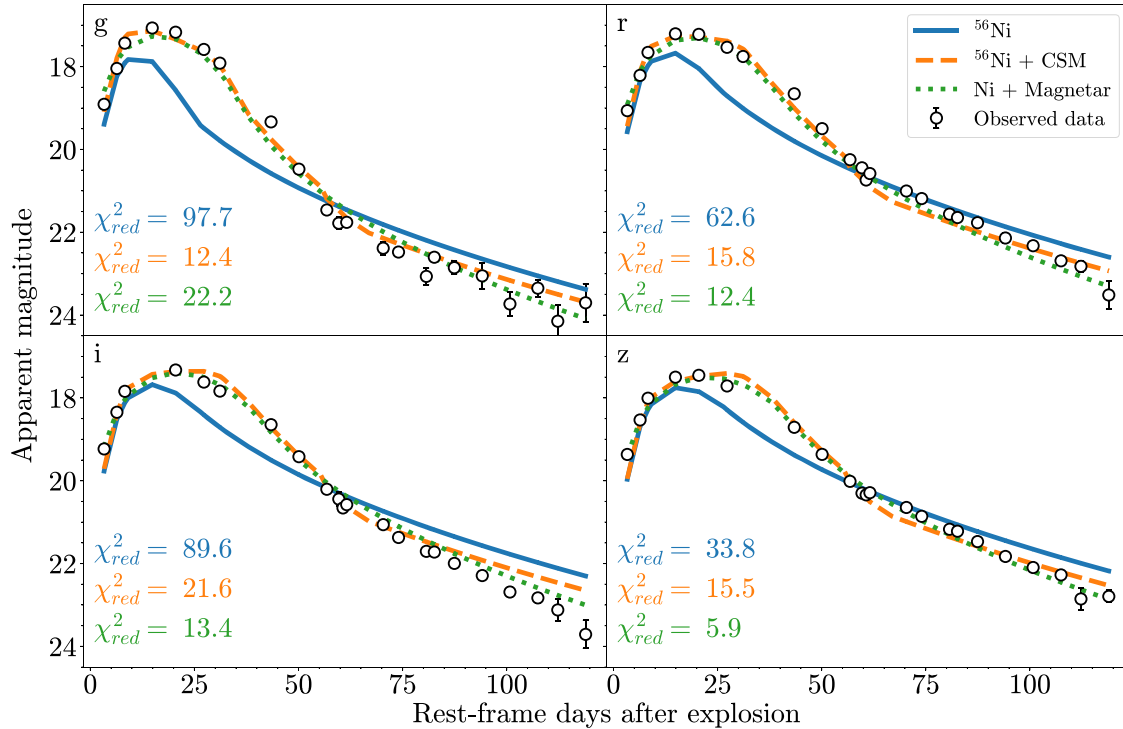
**Figure 8.** The best-fitting light curves to our observations for a variety of physical models after 10 000 MCMC iterations, along with the observed values in *griz* bands.

(i) Nickel–cobalt decay: The canonical model of an SN IIb, using the treatment of the radioactive decay of $^{56}$Ni and $^{56}$Co from Nadyozhin (1994).

(ii) Nickel–cobalt decay + CSM interaction: The nickel–cobalt decay model above along with extra luminosity resulting from interaction of the ejecta with a surrounding CSM, using the model from Chatzopoulos et al. (2013). Although we do not observe the narrow spectral features associated with CSM interaction in DES14X2fna, this does not rule out the possibility that CSM interaction occurred. Given a sufficiently low-density CSM (Reynolds et al. 2020), or if the SN ejecta collides with the CSM outside the broad-line-forming region (Arcavi et al. 2017a), CSM interaction can occur without clear narrow-line spectral features.

(iii) Nickel–cobalt decay + magnetar: SN driven by a combination of nickel–cobalt decay, using the model outlined above, and a magnetar, using the model from Nicholl, Guillochon & Berger (2017). This is the proposed model for SN 1998bw in Wang et al. (2017), which shows a close resemblance to DES14X2fna at peak. It is also suggested as an explanation for the light curve of ASASSN-18am in Bose et al. (2020).

For each of these models, we run an MCMC-based MOSFiT simulation comprising 1000 walkers for 10 000 iterations. Each model utilizes the PHOTOSPHERES.TEMPERATURE_FLOOR photospheric model as outlined in Nicholl et al. (2017). For each walker, MOSFiT calculates model photometry at each epoch and compares with observed photometry – we use model and observed photometry to calculate the reduced $\chi^2$ value, $\chi^2_{\rm red}$ and use this to identify the best-fitting model to observations. For these model fits, we have assumed a fixed opacity to UVOIR radiation $\kappa = 0.07$ cm$^2$ g$^{-1}$, following Prentice et al. (2019), as well as a fixed opacity to $\gamma$-rays produced in $^{56}$Ni decay of $\kappa_{\gamma, \rm Ni} = 0.03$ cm$^2$ g$^{-1}$ (Wang et al. 2017). Corner

plots of each model fit are shown in Appendix A (supplementary material). Fig. 8 shows the best-fitting light curve for each of these methods in DES *griz* bands, along with the reduced $\chi^2$ value for each of these fits in each band.

It is clear that nickel–cobalt decay alone is unable to accurately model the light curve of DES14X2fna, with an overall $\chi^2_{\rm red} = 58.2$. This model predicts a narrower peak in the *r* band and a slower tail decline rate, especially in higher wavelength bands, than our observations. Additionally, this model overall underestimates luminosity in the *r* band and overestimates at late times in longer wavelength bands suggesting that it also fails to fit the high temperature and slow temperature decline of DES14X2fna. The full corner plot of this fit is presented in Appendix A1 (supplementary material), Fig. A1, but in brief this model fails to give a reasonable value of ejecta mass and is consistent with a value below our chosen lower limit of 1 M$_\odot$. Prolonged H features in spectroscopy of DES14X2fna indicate a more massive hydrogen envelope than the prototypical SN IIb SN 1993J, suggesting that the ejecta mass cannot be substantially smaller than other objects – this motivated our choice of lower limit and and rules out such a low value. This was obtained even when using a Gaussian prior with a mean and standard deviation of 3 and 0.3 M$_\odot$, respectively, selected arbitrarily to try and force the model to identify a minimum with a physically reasonable ejecta mass. Overall, this model is unable to match our observations and does not have realistic best-fitting values for all parameters.

The addition of CSM-interaction to the nickel–cobalt decay model, however, significantly improves the quality of the model, with a reduced $\chi^2$ of 12.1. This model fits both the peak and the decline much more accurately, although the decline rate is still slower than observed in higher wavelength bands. The best-fitting ejecta mass is $2.69^{+0.16}_{-0.28}$ M$_\odot$, very typical for an SN IIb based on the sample in Prentice et al. (2019). This model fits kinetic energy rather than

ejecta velocity directly, but using the best-fitting kinetic energy of $1.71^{+0.18}_{-0.20} \times 10^{51}$ erg s$^{-1}$ along with the ejecta mass, we estimate an ejecta velocity of ~8000 km s$^{-1}$, comparable to our velocities inferred from spectroscopy. This model is able to match most features of our observed photometry and the physical parameter values are consistent with properties expected for an SN IIb.

The addition of a magnetar to nickel-cobalt decay further improves the quality of the fit, with a reduced $\chi^2$ of 10.0. Compared with the CSM model, this model matches the observed decline rate of DES14X2fna in the tail more accurately. The best-fitting ejecta mass is $2.85^{+0.61}_{-0.55}$ M$_\odot$, also very typical for an SN IIb compared with the Prentice et al. (2019) sample. For this fit, we have assumed a fixed value of $\kappa_{\gamma,\,\mathrm{mag}} = 0.01$ cm$^2$ g$^{-1}$. We did experiment with leaving this as a free parameter but the MCMC favoured a value below the range of expected values for a magnetar, between $10^{-2}$ and $10^6$ cm$^2$ g$^{-1}$ (Kotera, Phinney & Olinto 2013). As a result, we fix this to the lowest value considered reasonable.

As an independent check, we also considered an alternative semi-analytic magnetar code based on the model outlined in Inserra et al. (2013, hereafter I13). Unlike MOSFiT, I13 fits directly to bolometric luminosities rather than observed photometry – as such, we utilize our blackbody estimated luminosities from Section 3.3. For this fit, we have again assumed a fixed value of $\kappa_{\gamma,\,\mathrm{mag}} = 0.01$ cm$^2$ g$^{-1}$. Our fit to these data using I13 is shown in Fig. 9 – overall, this model does provide us with a good fit to our data both around peak and in the tail.

As previously noted, the *r*-band light curve of DES14X2fna shows strong resemblance around peak to that of SN 1998bw (SN Ic-BL), which Wang et al. (2017) find can be accurately fit with a combination of a magnetar and nickel-cobalt decay. Our MOSFiT and I13 magnetar fits indicate that a similar mechanism could power DES14X2fna. Table 8 shows the best-fitting properties of our magnetar model fit for DES14X2fna along with those of SN 1998bw. For both models, the predicted initial ejecta velocity $v_{\mathrm{ejecta}}$ is consistent with our velocity measurements from spectroscopy and the ejecta mass is consistent with the SNe IIb population in Prentice et al. (2019). Comparing DES14X2fna to SN 1998bw, there are differences of a factor of ~2–2.5 for the estimated values of magnetar magnetic field strength and spin period. Ejecta velocity is lower for DES14X2fna although only by less than $1.5\sigma$, and the ejecta mass is comparable for both objects. One key difference between the two objects is that for DES14X2fna, the $^{56}$Ni mass is considerably less than for SN 1998bw. The quoted $^{56}$Ni mass for I13, <0.023 M$_\odot$, is a $1\sigma$ upper limit from the fitting uncertainty – the parameter value itself is ~$10^{-4}$. Under the assumption that DES14X2fna is powered in part by a magnetar, this demonstrates that the contribution of $^{56}$Ni decay to the light curve is minimal. The different magnetar properties of DES14X2fna compared to SN 1998bw have the effect of increasing the initial energy output of the magnetar and increasing the time-scale over which it declines. This leads to DES14X2fna and SN 1998bw showing similar light-curve peaks before DES14X2fna declines far more rapidly at later times.

## 5 DISCUSSION

### 5.1 Peak luminosity

By studying both the *r* band and bolometric light curves of DES14X2fna, we have demonstrated that it is considerably more luminous than any other SN IIb in our comparison sample with the exception of ASASSN-18am. Under the assumption that this object follows the canonical $^{56}$Ni decay model for an SN IIb, the

peak must be powered by a very considerable mass of $^{56}$Ni far in excess of what is typical for an SN IIb. Using our bolometric light curve for DES14X2fna we can make some initial estimates of the mass of $^{56}$Ni synthesized in the explosion. Equation (3) of Prentice et al. (2016) from the commonly used, analytically derived 'Arnett model' (Arnett 1982) allows us to estimate the $^{56}$Ni mass using the peak bolometric luminosity, $L_p$, and the rise time to peak bolometric luminosity, $t_p$. Using our values for these from Section 3.3 gives an estimate of $M_{\mathrm{Ni}} = 1.02 \pm 0.20$ M$_\odot$. Please note this is not a Gaussian uncertainty, rather a maximum possible deviation based on our uncertainty in explosion epoch, constrained only between the last non-detection and first detection. Equation (19) of Khatami & Kasen (2019) proposes an updated relation between peak time and luminosity, with the effect of opacity and mixing encapsulated in a parameter $\beta$. Assuming that the proposed $\beta$ value for SNe IIb in Khatami & Kasen (2019), 0.82, is valid for DES14X2fna, we obtain $M_{\mathrm{Ni}} = 0.633^{+0.083}_{-0.079}$ M$_\odot$. Again, this is not a Gaussian uncertainty, instead reflecting the maximum possible deviation due to uncertainty in explosion epoch. Meza & Anderson (2020) find SNe IIb and Ib $^{56}$Ni masses that typically vary from ~0.03–0.2 and ~0.02–0.13 M$_\odot$ using these methods, respectively. DES14X2fna would require a $^{56}$Ni mass that is approximately four to five times larger than is typical for SNe IIb.

The breadth of the peak of the light curve of DES14X2fna also indicates an ejecta mass at the very least typical for an SN IIb. We can estimate the ejecta mass using equation (1) in Prentice et al. (2019), based on the Arnett model,

$$M_{\mathrm{ej}} = \frac{1}{2}\left(\frac{\beta c}{\kappa}\right)\tau_m^2 v_{\mathrm{sc}}, \qquad (1)$$

where $\beta \approx 13.7$ is a constant of integration, $\kappa$ is the opacity of the ejecta, and $v_{\mathrm{sc}}$ is a characteristic velocity of the ejecta. We again follow Prentice et al. (2019) in assuming $\kappa = 0.07$ cm$^2$ g$^{-1}$ and $\tau_m = t_p$, and use the velocity of H$\alpha$ around peak of $\simeq$9000 km s$^{-1}$ as an estimate of the characteristic ejecta velocity. This gives an estimate for ejecta mass of $M_{\mathrm{ej}} = 2.35^{+1.11}_{-0.90}$ M$_\odot$, consistent with the mean and median $M_{ej}$ for SNe IIb in Prentice et al. (2019), $2.7 \pm 1.0$ and $2.5^{+1.3}_{-0.7}$ M$_\odot$, respectively. This suggests that the light curve of DES14X2fna is consistent with a fairly typical SN IIb ejecta mass.

### 5.2 Tail decline

As well as the high peak luminosity and broad peak of DES14X2fna, we have also demonstrated that DES14X2fna declines far more rapidly at late times than any other SN in our comparison sample. However, under the assumption that this object is powered by $^{56}$Ni decay, this creates a discrepancy with the very luminous peak of DES14X2fna.

In the canonical picture of an SN IIb, after any hydrogen present has recombined the light curve is driven by radioactive decay of $^{56}$Co, as any $^{56}$Ni produced will have already decayed. The source of optical luminosity at this stage is the deposition of $\gamma$-rays and positrons produced in the radioactive decay process. Under the assumption that $\gamma$-rays produced are fully trapped and all deposit their energy, the luminosity of the SN will decline at a rate of 0.98 mag (100 d)$^{-1}$ (Woosley, Pinto & Hartmann 1989). A decline rate faster than this indicates that $\gamma$-rays produced are not fully trapped and therefore some of their energy is not observed in the optical light curve. In *griz* photometric bands, DES14X2fna has decline rates of $3.96 \pm 0.45$, $4.30 \pm 0.10$, $5.15 \pm 0.13$, and $4.70 \pm 0.08$ mag (100 d)$^{-1}$, far in excess of the rate expected for complete trapping. Such a fast decline rate indicates a very low ejecta mass, allowing most of the
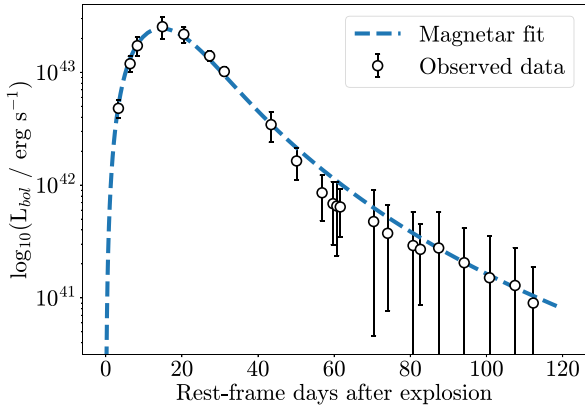
**Figure 9.** Bolometric luminosities of DES14X2fna calculated from blackbody fits to observed photometry along with a magnetar fit to this data based on the model detailed in I13.

$\gamma$-rays produced to escape. However, as discussed in Section 5.1, if DES14X2fna were to be powered by $^{56}$Ni it would require a mass of $^{56}$Ni at least four times that of any other SN IIb observed and an ejecta mass at least typical for an SN IIb. This high mass of material would lead to significant trapping of the $\gamma$-rays produced in $^{56}$Co decay and therefore preclude the fast decline that is observed in DES14X2fna. Assuming $^{56}$Ni alone, DES14X2fna cannot have an ejecta mass typical for an SN IIb while also displaying a significantly faster decline rate.

We can also estimate $^{56}$Ni mass from the bolometric tail decline, which helps to reiterate the discrepancy between peak and decline rate for DES14X2fna. For a canonical SN IIb, in this phase $^{56}$Ni mass will have almost entirely decayed and the light curve is powered solely by $^{56}$Co. Assuming complete $\gamma$-ray trapping, in this phase, the light curve will follow (Jerkstrand et al. 2012)

$$L(t) = 1.42 \times 10^{43} \frac{M_{\rm Ni}}{\rm M_\odot} (e^{-t/t_{\rm Co}} - e^{-t/t_{\rm Ni}}) \ {\rm erg\ s^{-1}}, \qquad (2)$$

where $L(t)$ is the luminosity, $M_{\rm Ni}$ is the mass of $^{56}$Ni synthesized in the explosion and $t_{\rm Co}$ and $t_{\rm Ni}$ are the characteristic decay timescales for $^{56}$Co and $^{56}$Ni, respectively. Assuming that other SNe follow this relation and have similar $\gamma$-ray deposition, SNe $^{56}$Ni masses will share the same ratio as bolometric luminosity at the same epoch. SN 1987A is commonly used for this analysis, although as it does not reach the linear decline phase of its light curve until after our last data for DES14X2fna, this method cannot be directly used. However, we can infer a bolometric luminosity at later times for DES14X2fna by extrapolating the linear decline in $\log(L_{\rm bol})$. After 159.1 d since explosion SN 1987A has a UV–optical–infrared (UVOIR) bolometric luminosity of $\log_{10}(L_{\rm UVOIR}/$ erg s$^{-1}$) $= 41.381$ (Suntzeff et al. 1991), whereas extrapolating

the light curve of DES14X2fna gives a luminosity at this epoch of $\log_{10}(L_{\rm bol}/$ erg s$^{-1}$) $= 40.22 \pm 0.11$. Note that the uncertainty for the SN 1987A luminosity is less than 0.02 dex, although no exact value is given. As a result, we consider its uncertainty to be negligible compared to DES14X2fna. The ratio of luminosities is $(6.93 \pm 1.74) \times 10^{-2}$, leading to an estimate for $^{56}$Ni mass for DES14X2fna of $(5.20 \pm 1.35) \times 10^{-3}$ M$_\odot$. The underlying assumption that these objects share similar $\gamma$-ray deposition is clearly not valid as DES14X2fna exhibits a very rapid decline not seen in SN 1987A, so this value is only a lower limit on the $^{56}$Ni mass produced. While only a lower limit, the fact that this value is nearly two orders of magnitude less than the mass of $^{56}$Ni predicted from peak luminosity demonstrates the inconsistency between peak and tail of DES14X2fna.

It is also possible to take into account the effect of incomplete trapping of $\gamma$-rays when estimating the $^{56}$Ni mass from the bolometric decline. Clocchiatti & Wheeler (1997) propose a simple model to take this into account, also given in equation (2) of Terreran et al. (2016). This is the most logical method to estimate $^{56}$Ni mass for DES14X2fna, given its fast decline rate. However, we find that this model is unable to constrain the $^{56}$Ni mass of DES14X2fna despite working for every other object in our SNe IIb comparison sample. The reason for this appears to be that DES14X2fna declines too fast to be well fit by this model. Equation (7) of Clocchiatti & Wheeler (1997),

$$\frac{\rm d}{{\rm d}t} m(t) = \frac{\rm d}{{\rm d}t} m_0(t) + \frac{5 \log_{10}(e)}{e^{(T_0/t)^2} - 1} \frac{T_0^2}{t^3}, \qquad (3)$$

gives an expression for the decline rate in magnitude for $^{56}$Co decay, where $({\rm d}/{\rm d}t)m_0(t)$ is the decline rate for fully trapped $^{56}$Co decay, 0.98 mag (100 d)$^{-1}$, $T_0$ is the characteristic decay time for the $\gamma$-ray optical depth and the complete second term corresponds to the shift in decline rate as a result of incomplete trapping, $({\rm d}/{\rm d}t)m_1(t)$. If we are to assume a fixed value of $t$, the second term increases with decreasing $T_0$ and is maximized in the limit $T_0$ tends to zero. Applying this, the maximum value of the second term is

$$\lim_{x \to 0} \frac{\rm d}{{\rm d}t} m_1(t) = \frac{5 \log_{10}(e)}{t}.$$

At the start of the tail after 60 d, this term is 3.62 mag (100 d)$^{-1}$, giving a maximum decline rate of 4.60 mag (100 d)$^{-1}$, which does not rule out the fast decline rate of DES14X2fna at this epoch. However, at later times the maximum decline rate decreases – for example, 100 d after explosion the maximum possible decline rate is 3.15 mag (100 d)$^{-1}$, which is more than 1 mag (100 d)$^{-1}$ less than the observed decline rate of DES14X2fna at this epoch. This discrepancy only increases at later stages of our observed light curve. Overall, this suggests that DES14X2fna declines too rapidly to be explained by $^{56}$Ni decay alone.

**Table 8.** The best-fitting properties of the combined magnetar and $^{56}$Ni fit to photometry of DES14X2fna using both MOSFiT and I13, along with the best-fitting magnetar properties of SN 1998bw from Wang et al. (2017).

| SN | $B$ $(10^{14}$ G) | $P_{\rm spin}$ (ms) | $M_{\rm ejecta}$ (M$_\odot$) | $v_{\rm ejecta}$ $(10^3$ km s$^{-1}$) | $M_{\rm Ni}$ (M$_\odot$) | $\kappa_{\gamma,\,{\rm mag}}$ (cm$^2$ g$^{-1}$) |
|---|---|---|---|---|---|---|
| DES14X2fna (MOSFiT) | $8.70^{+6.24}_{-2.26}$ | $8.22^{+1.86}_{-2.69}$ | $2.85^{+0.61}_{-0.55}$ | $8.90^{+0.45}_{-0.43}$ | $(4.41^{+6.87}_{-3.25}) \times 10^{-3}$ | $0.01^b$ |
| DES14X2fna (I13) | $7.80 \pm 2.32$ | $11.96 \pm 0.28$ | $2.10 \pm 0.43$ | $9.04 \pm 2.22$ | $<0.023^a$ | $0.01^b$ |
| SN 1998bw | $16.6^{+2.1}_{-1.4}$ | $20.8 \pm 0.8$ | $2.6^{+0.5}_{-0.4}$ | $11.05^{+1.50}_{-1.59}$ | $0.10^{+0.03}_{-0.02}$ | $0.29^{+0.19}_{-0.17}$ |

$^a$1$\sigma$ upper limit
$^b$Fixed value.

### 5.3 Power source

Throughout this paper, we have demonstrated that DES14X2fna has very different properties when compared with other SNe IIb. DES14X2fna reaches a peak absolute magnitude in the *r* band of −19.37, comparable only to ASASSN-18am and nearly 1 mag brighter than any other SN IIb. DES14X2fna also displays a relatively broad light-curve peak. As discussed in Section 5.1, this is indicative of a very high $^{56}$Ni mass and an at least comparable ejecta mass when compared to other SNe IIb. However, as discussed in Section 5.2, these $^{56}$Ni and ejecta masses are not consistent with the very fast post-peak decline observed across all photometric bands of DES14X2fna. DES14X2fna appears to decline too rapidly for this to be explained simply by incomplete trapping of $\gamma$-rays produced in $^{56}$Co decay. In Section 4, we consider a semi-analytic model of $^{56}$Ni decay. This model is unable to accurately model the light curve of DES14X2fna, predicting a narrower peak in the *r* band and a slower tail decline rate, especially in higher wavelength bands, than our observations. This model is also unable to reproduce the temperature of DES14X2fna, underestimating luminosity at peak in shorter wavelength bands and overestimating at longer wavelengths at later times. Based on the contradictions between the peak and decline of the light curve of DES14X2fna as well as the inability of the semi-analytic model to fit observed photometry, we rule out the possibility that DES14X2fna can be powered by $^{56}$Ni decay alone.

Having established that DES14X2fna requires an additional source of luminosity besides $^{56}$Ni, the question to address is what that source of luminosity might be. One possibility is that interaction with a surrounding CSM helps to power the light curve. Such a model allows for a faster decline than $^{56}$Ni decay alone as the decline rate is no longer limited by the decay time-scale of $^{56}$Co – a decrease in the luminosity from CSM interaction can lead to a much more rapid decline (Taubenberger et al. 2019). There is precedent for SNe IIb that also show signs of interaction. SN 2018gjx (Prentice et al. 2020) was an object that spectroscopically resembled an SN IIb before going on to show narrow spectral features typical of an SN Ibn after ∼40 d, although DES14X2fna is two mags brighter at peak and does not show narrow spectral features during our spectroscopic coverage so is not directly comparable. Our semi-analytic fits using MOSFiT suggest that CSM interaction combined with $^{56}$Ni decay could power the light curve of DES14X2fna. Although we do not see the narrow spectral features associated with CSM interaction in spectroscopy of DES14X2fna, as previously mentioned this does not rule out that it occurred – interaction has been invoked for other objects that no not display narrow lines (e.g. iPTF14hls, Arcavi et al. 2017a; SN 2016gsd, Reynolds et al. 2020).

We have also shown that the *r*-band peak of DES14X2fna shows close resemblance to the *R*-band peak of SN 1998bw, potentially suggesting that they share a source of luminosity at this phase of the light curve. However, DES14X2fna is also seen to decline far more rapidly than SN 1998bw at late times. If they are to share a source of luminosity, this source must be capable of powering the peak before quickly decreasing in luminosity. Wang et al. (2017) find that the bolometric light curve of SN 1998bw is likely powered by a combination of $^{56}$Ni decay and a magnetar, with this model favoured over the traditional two-component model for SNe Ic-BL as it can explain the late-time shift in decline rate. Crucially, Wang et al. (2017) find that the magnetar dominates the light curve only during peak and at very late times, with the post-peak decline dominated by $^{56}$Ni decay. The very luminous peak and fast decline of DES14X2fna could therefore potentially be explained by a magnetar. Our semi-analytic model fits find that a combination of a magnetar and $^{56}$Ni decay is able to fit the light curve of DES14X2fna far better

than $^{56}$Ni decay, accurately modelling the peak and decline rate of DES14X2fna.

The similarity of DES14X2fna to SN 1998bw and the good fit to our observed photometry given by the combined magnetar and $^{56}$Ni model provides evidence that DES14X2fna could also partially be powered by a magnetar. This model also demonstrates that $^{56}$Ni makes a minimal contribution to the light curve. This helps to explain the differences between DES14X2fna and SN 1998bw. As shown in Wang et al. (2017), the light curve of SN 1998bw is dominated by a magnetar only around peak and at very late times, far later than photometry is available for DES14X2fna. At intermediate times, the light curve is dominated by $^{56}$Co decay. In the case of DES14X2fna, it may be that the light curve is still dominated by a magnetar at intermediate times, which would allow for a faster decline rate than is typically associated with $^{56}$Co decay. This would explain why DES14X2fna declines far more rapidly after peak than SN 1998bw. Overall, a magnetar model provides a good fit to our observations of DES14X2fna.

An additional possibility to consider is whether the rapid decline of DES14X2fna could result from the onset of dust formation. This process has been invoked to explain fast declines observed in SNe Ibn such as SN 2006jc (Anupama et al. 2008). For this object, the optical light curve was seen to flatten ∼30–50 d after maximum before a sudden increase in optical decline rate was accompanied by an increase in NIR luminosity as a result of dust reprocessing. In the absence of NIR observations for DES14X2fna we cannot be sure whether this might have occurred, although it is important to note that SN 2006jc was an object that showed strong interaction and had a much faster evolution than DES14X2fna – even during the flattening phase, it still declined faster than DES14X2fna at optical wavelengths. As a result, we consider the possibility that this decline rate is due to dust formation unlikely although we cannot rule it out.

### 5.4 DES14X2fna as a photometric contaminant

DES14X2fna has a very high luminosity at peak, reaching a peak $M_r \simeq$ -19.3, and therefore into the range of peak luminosities expected for SNe Ia. While the H and He features of DES14X2fna clearly distinguish it from an SN Ia, it is a possibility that a similar object could be mistakenly included in a photometric sample of SNe Ia in the absence of spectroscopy. To assess this, we use the SNe Ia light curve template fitter SALT2 (Guy et al. 2007) to fit our observed photometry using the PYTHON package SNCOSMO. SALT2 calculates the stretch and colour parameters for an SN Ia light curve, $x_1$ and $c$. For the DES cosmological sample of SNe Ia, only SNe with $-0.3 < c < 0.3$ and $-3 < x_1 < 3$ are included. Fitting the observed light curve between $-15$ and $+45$ d relative to explosion gives a poor quality fit, particularly in higher wavelength bands, with $\chi^2_{\rm red} = 6041$. This fit also has a value of $x_1 = -3.08$ and $c = -1.20$, meaning that it would not pass the cuts to be included in a cosmological sample. However, the large $\chi^2_{\rm red}$ value obtained also results partly from the fact that DES14X2fna has very high signal-to-noise data. If a similar object were observed at a higher redshift, it is possible that it could be misclassified as an SN Ia.

To assess the likelihood of an object similar to DES14X2fna acting as a photometric contaminant, we simulate the object based on SED templates from Hounsell et al. (in preparation) over the 5 yr of DES using SNANA (Kessler et al. 2009). These templates can extend into the UV based on extrapolation of the optical SED but effects such as line blanketing mean that these are not reliable. As a result, we simulate objects up to $z < 0.59$ meaning that the effective wavelength of DES *g* band never falls below 3000 Å. In total, 23 870

DES14X2fna-like events are simulated at different redshifts in DES up to the this limit. Each of these synthetic light curves is fit using SALT2, a standard template fitter for SNe Ia light curves (Guy et al. 2007), and the recurrent neural network (RNN)-based photometric classifier SUPERNNOVA (M'oller & de Boissière 2019) is used to estimate the probability that each light curve corresponds to an SN Ia, hereafter referred to as $P_{Ia}$. The model used for classification was trained on a set of templates that did not include DES14X2fna and so has not previously seen an object with these properties. To identify the synthetic light curves with the potential to be mistakenly included in cosmological samples of SNe Ia, we apply a number of cuts:

(i) Select only SNe with valid SALT2 fits: This identifies SNe with light curves with the potential to be included in the DES 3-yr cosmological sample based on the cuts outlined in Brout et al. (2019). Any objects outside the redshift range of [0.05,1.2], with a Milky Way $E(B − V) > 0.25$, without data both before and after peak or without data points with a signal-to-noise ratio $> 5$ in at least two bands are excluded from the SALT2 fits entirely, leaving a total of 18 520 objects.

(ii) Select only SNe with $−0.3 < c < 0.3$ and $−3 < x_1 < 3$ based on SALT2 fits: As previously mentioned, this cut is used in Brout et al. (2019) to select the cosmological sample. Performing this cut leaves a total of 15 101 objects in the sample.

(iii) Select only SNe with a high value of $P_{Ia}$: This identifies only the synthetic SNe with a high probability of being classified as an SN Ia by SUPERNNOVA. Note that SUPERNNOVA has two models, one for photometric classification with a host spectroscopic redshift and one without. Here we consider only the model for classification with a redshift as objects without host redshifts would not be included in a cosmological sample. This confidence threshold for inclusion is arbitrary – a lower threshold will give a larger sample but increases the likelihood of sources being included incorrectly. Using a high threshold of $P_{Ia} > 0.9$ gives a total of 270 synthetic SNe that would be misclassified as SNe Ia, 1.1 per cent of the sample. Lowering this threshold to 0.8 increases the number of misclassifications to 372, 1.6 per cent of the sample. At a threshold of $P_{Ia} > 0.5$, where an object is simply more likely than not to be an SN Ia, there are 565 misclassifications corresponding to 2.4 per cent of the sample.

Overall, in our simulations a DES14X2fna-like object is misclassified as an SN Ia in ∼1.1–2.4 per cent cases depending on the threshold used for $P_{Ia}$. While rare, it does show that such an object does have the potential to contaminate a cosmological sample. Analysing the light curves of the synthetic SNe that were classified shows that this generally occurs when the fast linear decline of DES14X2fna is undetected, due to either dropping below the detection limit of the survey or the end of the observing season, or is observed with very low signal-to-noise ratio. This suggests that DES14X2fna is difficult to differentiate from an SN Ia based on photometry around peak, but can be differentiated from its late-time decline. This is to be expected given DES14X2fna does not show the second peak typical for SNe Ia and has a very fast tail decline.

Given that DES14X2fna is near unique, it is clear that this type is rare with a rate only a small fraction of the rate of SNe Ia. In addition to this, only a small fraction of similar events will be misclassified as SNe Ia. While DES14X2fna is an interesting case of a potential contaminant, in practice, the effect that these objects have on cosmological analyses is unlikely to be significant.

## 6 CONCLUSIONS

DES14X2fna is an unusual SN IIb with both a very high peak luminosity and very fast late-time decline compared to other SNe IIb. At peak, this SN reaches an *r*-band absolute magnitude of $−19.37 ± 0.05$, comparable to the recently discovered very luminous SN IIb ASASSN-18am and 0.88 mag brighter than any other SN IIb. The light curve is also fairly broad for an SN IIb. Our main conclusions are as follows:

(i) The light curve of DES14X2fna cannot be explained by $^{56}$Ni decay alone. The peak luminosity and peak time of DES14X2fna indicate a $^{56}$Ni mass synthesized in the explosion more than four times greater than observed in any other SNe IIb in Khatami & Kasen (2019) and an ejecta mass of $2.35^{+1.11}_{-0.90}$ $M_{\odot}$, which is consistent with other SNe IIb in Prentice et al. (2019). However, DES14X2fna declines at more than three times the rate expected for fully trapped $^{56}$Co decay in the *g* band and more than four times in *riz* bands. This decline is more than 1 mag 100 d$^{-1}$ faster than any other SN IIb in the tail.

(ii) DES14X2fna displays signs of H for far longer than the prototypical SN IIb SN 1993J, indicating it has a more massive H envelope than a typical SN IIb. Bose et al. (2020) obtains a similar finding for ASASSN-18am.

(iii) Our semi-analytic $^{56}$Ni decay models using MOSFiT are unable to fit the peak and the fast tail decline of the light curve of DES14X2fna.

(iv) DES14X2fna declines too rapidly at late times to be fit by the treatment for incomplete trapping of $\gamma$-rays produced in $^{56}$Co decay in Clocchiatti & Wheeler (1997), providing further evidence that an additional source of luminosity is required.

(v) The addition of CSM interaction to the $^{56}$Ni decay model provides a significantly better fit to the observed photometry of DES14X2fna than $^{56}$Ni decay alone, indicating that it could in part power this object.

(vi) The light curve of DES14X2fna is well fit by a magnetar model. DES14X2fna also shows resemblance to SN 1998bw around peak, which is well fit by a magnetar model in Wang et al. (2017).

(vii) Based on simulations of DES14X2fna in SNANA using templates from Hounsell et al. (in preparation) in DES, we find that such an object is misclassified as an SN Ia suitable for cosmology in ∼1.1–2.4 per cent cases depending on the probability threshold used. This typically occurs when the fast decline of such an object is not observed with sufficient signal-to-noise ratio. However, given the rarity of such events, they are unlikely to act as a significant contaminant to cosmological samples.

## DATA AVAILABILITY STATEMENT

The data underlying this study regarding DES14X2fna are available in this paper and through the WISeREP (https://wiserep.weizmann.ac.il/home) archive (Yaron & Gal-Yam 2012). Comparison data were sourced from published literature with sources detailed in Tables 5 and 6.

## REFERENCES

Aldering G., Humphreys R. M., Richmond M., 1994, AJ, 107, 662
Ambikasaran S., Foreman-Mackey D., Greengard L., Hogg D. W., O'Neil M., 2015, IEEE Trans. Pattern Anal. Mach. Intell., 38, 252
Anderson J. P., Covarrubias R. A., James P. A., Hamuy M., Habergham S. M., 2010, MNRAS, 407, 2660
Angus C. R. et al., 2019, MNRAS, 487, 2215
Anupama G. C., Sahu D. K., Gurugubelli U. K., Prabhu T. P., Tominaga N., Tanaka M., Nomoto K., 2008, MNRAS, 392, 894
Arcavi I. et al., 2017a, Nature, 551, 210
Arcavi I. et al., 2017b, ApJ, 837, L2
Arnett W. D., 1982, ApJ, 253, 785
Barbon R., Benetti S., Cappellaro E., Patat F., Turatto M., Iijima T., 1995, A&AS, 110, 513
Benson P. J. et al., 1994, AJ, 107, 1453
Bernstein J. P. et al., 2012, ApJ, 753, 152
Bersten M. C. et al., 2012, ApJ, 757, 31
Bersten M. C. et al., 2018, Nature, 554, 497
Bianco F. B. et al., 2014, ApJS, 213, 19
Bose S. et al., 2020, MNRAS, 503, 3472
Brout D. et al., 2019, ApJ, 874, 150
Brown P. J., Breeveld A. A., Holland S., Kuin P., Pritchard T., 2014, Ap&SS, 354, 89
Bruzual G., Charlot S., 2003, MNRAS, 344, 1000
Bufano F. et al., 2014, MNRAS, 439, 1807
Cano Z. et al., 2011, ApJ, 740, 41
Cappellari M., 2017, MNRAS, 466, 798
Cappellari M., Emsellem E., 2004, PASP, 116, 138
Cappellari M. et al., 2012, Nature, 484, 485
Chabrier G., 2003, PASP, 115, 763
Chatzopoulos E., Wheeler J. C., Vinko J., Horvath Z. L., Nagy A., 2013, ApJ, 773, 76
Childress M. J. et al., 2017, MNRAS, 472, 273
Chu J., Li W., Filippenko A. V., Blondin S., Narayan G., 2008, Cent. Bur. Electr. Telegrams, 1271, 1
Ciabattari F., Mazzoni E., 2011, Cent. Bur. Electr. Telegrams, 2827, 1
Clocchiatti A., Wheeler J. C., 1997, ApJ, 491, 375
Dopita M. A., Kewley L. J., Sutherland R. S., Nicholls D. C., 2016, Ap&SS, 361, 61
Drake A. J. et al., 2009, ApJ, 696, 870
Drout M. R. et al., 2011, ApJ, 741, 97
Eldridge J. J., Tout C. A., 2004, MNRAS, 353, 87
Ergon M. et al., 2015, A&A, 580, A142
Filippenko A. V., 1997, ARA&A, 35, 309
Fitzpatrick E. L., Massa D., 2007, ApJ, 663, 320
Flaugher B. et al., 2015, AJ, 150, 150
Folatelli G. et al., 2014, ApJ, 793, L22
Foley R. J. et al., 2003, PASP, 115, 1220
Fox O. D. et al., 2014, ApJ, 790, 17
Fremling C. et al., 2016, A&A, 593, A68

Gal-Yam A., Observational and Physical Classification of Super-novae,Handbook of Supernovae, 2017, Cham, p. 1.

Gal-Yam A., Ofek E. O., Shemmer O., 2002, MNRAS, 332, L73

Galama T. J. et al., 1998, Nature, 395, 670

Galbany L. et al., 2016, AJ, 151, 33

Galbany L. et al., 2018, ApJ, 855, 107

Graham M. L., Clubb K. I., Mauerhan J., Filippenko A. V., Serduke F. J. D., Nugent P. E., 2014, Astron. Telegram, 6591, 1

Guillochon J., Nicholl M., Villar V. A., Mockler B., Narayan G., Mandel K. S., Berger E., Williams P. K. G., 2018, ApJS, 236, 6

Guy J. et al., 2007, A&A, 466, 11

Helou G., Kasliwal M. M., Ofek E. O., Arcavi I., Surace J., Gal-Yam A., 2013, ApJ, 778, L19

Hicken M. et al., 2017, ApJS, 233, 6

Inserra C. et al., 2013, ApJ, 770, 128 (I13)

Japelj J., Vergani S. D., Salvaterra R., Renzo M., Zapartas E., de Mink S. E., Kaper L., Zibetti S., 2018, A&A, 617, A105

Jerkstrand A., Fransson C., Maguire K., Smartt S., Ergon M., Spyromilio J., 2012, A&A, 546, A28

Kasen D., Bildsten L., 2010, ApJ, 717, 245

Kato T., Uemura M., Ishioka R., Nogami D., Kunjaya C., Baba H., Yamaoka H., 2004, PASJ, 56, S1

Kerzendorf W. E. et al., 2019, A&A, 623, A34

Kessler R. et al., 2009, PASP, 121, 1028

Kewley L. J., Geller M. J., Jansen R. A., 2004, AJ, 127, 2002

Khatami D. K., Kasen D. N., 2019, ApJ, 878, 56

Kilpatrick C. D. et al., 2016, Astron. Telegram, 9536, 1

Kochanek C. S., 2018, MNRAS, 473, 1633

Kotera K., Phinney E. S., Olinto A. V., 2013, MNRAS, 432, 3228

Kuehn K., Lidman C., Martini P., Mudd D., Zhang B., Yuan F., 2014, Astron. Telegram, 6789, 1

Kumar B. et al., 2013, MNRAS, 431, 308

Lennarz D., Altmann D., Wiebusch C., 2012, A&A, 538, A120

Lewis J. R. et al., 1994, MNRAS, 266, L27

Lidman C. et al., 2020, MNRAS, 496, 19

Lyman J. D., Bersier D., James P. A., 2013, MNRAS, 437, 3848

M'oller A., de Boissière T., 2019, MNRAS, 491, 4277

Maeda K., Mazzali P. A., Deng J., Nomoto K., Yoshii Y., Tomita H., Kobayashi Y., 2003, ApJ, 593, 931

Maeda K. et al., 2015, ApJ, 807, 35

Maguire K. et al., 2012, MNRAS, 426, 2359

Metlova N. V., Tsvetkov D. Y., Shugarov S. Y., Esipov V. F., Pavlyuk N. N., 1995, Astron. Lett., 21, 598

Meza N., Anderson J. P., 2020, A&A, 641, A177

Mikuz H., Dintinjana B., Zwitter T., 1993, IAU Circ., 5796, 2

Modjaz M., Gutiérrez C. P., Arcavi I., 2019, Nat. Astron., 3, 717

Modjaz M. et al., 2020, ApJ, 892, 153

Monard L. A. G., 2009, Cent. Bur. Electr. Telegrams, 2071, 1

Morales-Garoffolo A. et al., 2014, MNRAS, 445, 1647

Moriya T. J., Maeda K., Taddia F., Sollerman J., Blinnikov S. I., Sorokina E. I., 2013, MNRAS, 435, 1520

Nadyozhin D. K., 1994, ApJS, 92, 527

Nakar E., Piro A. L., 2014, ApJ, 788, 193

Nicholl M., Guillochon J., Berger E., 2017, ApJ, 850, 55

Nicholls B. et al., 2016, Astron. Telegram, 9521, 1

Nomoto K. I., Iwamoto K., Suzuki T., 1995, Phys. Rep., 256, 173

Ofek E. O. et al., 2014, ApJ, 789, 104

Okyudo M., Kato T., Ishida T., Tokimasa N., Yamaoka H., 1993, PASJ, 45, L63

Osterbrock D. E., 1989, Astrophysics of Gaseous Nebulae and Active Galactic Nuclei. University Science Books, Mill Valley, California

Pandey S. B., Anupama G. C., Sagar R., Bhattacharya D., Sahu D. K., Pandey J. C., 2003, MNRAS, 340, 375

Papadopoulos A. et al., 2015, MNRAS, 449, 1215

Pastorello A. et al., 2008, MNRAS, 389, 955

Patat F. et al., 2001, ApJ, 555, 900

Pessi P. J. et al., 2019, MNRAS, 488, 4239

Pettini M., Pagel B. E. J., 2004, MNRAS, 348, L59

Pignata G. et al., 2009, Cent. Bur. Electr. Telegrams, 1663, 1

Pignata G. et al., 2011, ApJ, 728, 14

Piro A. L., 2015, ApJ, 808, L51

Prentice S. J. et al., 2016, MNRAS, 458, 2973

Prentice S. J. et al., 2018, MNRAS, 478, 4162

Prentice S. J. et al., 2019, MNRAS, 485, 1559

Prentice S. J. et al., 2020, MNRAS, 499, 1450

Pugh H., Park S., Li W., 2004, IAU Circ., 8425, 1

Qiu Y., Li W., Qiao Q., Hu J., 1999, AJ, 117, 736

Rasmussen C. E., Williams C. K. I., 2005, Gaussian Processes for Machine Learning (Adaptive Computation and Machine Learning). The MIT Press,Cambridge, Massachusetts

Reynolds T. M. et al., 2020, MNRAS, 493, 1761

Richmond M. W., Treffers R. R., Filippenko A. V., Paik Y., Leibundgut B., Schulman E., Cox C. V., 1994, AJ, 107, 1022

Richmond M. W., Treffers R. R., Filippenko A. V., Paik Y., 1996, AJ, 112, 732

Ryder S. D. et al., 2018, ApJ, 856, 83

Sahu D. K., Tanaka M., Anupama G. C., Gurugubelli U. K., Nomoto K., 2009, ApJ, 697, 676

Sahu D. K., Anupama G. C., Chakradhari N. K., 2013, MNRAS, 433, 2

Sahu D. K., Anupama G. C., Chakradhari N. K., Srivastav S., Tanaka M., Maeda K., Nomoto K., 2018, MNRAS, 475, 2591

Sapir N., Waxman E., 2017, ApJ, 838, 130

Schlafly E. F., Finkbeiner D. P., 2011, ApJ, 737, 103

Schulze S. et al., 2020, preprint (arXiv:2008.05988)

Smith M. et al., 2016, ApJ, 818, L8

Smith M. et al., 2020, MNRAS, 494, 4426

Sollerman J., Kozma C., Fransson C., Leibundgut B., Lundqvist P., Ryde F., Woudt P., 2000, ApJ, 537, L127

Sollerman J. et al., 2002, A&A, 386, 944

Stritzinger M. D. et al., 2018, A&A, 609, A134

Suntzeff N. B., Phillips M. M., Depoy D. L., Elias J. H., Walker A. R., 1991, AJ, 102, 1118

Szalai T. et al., 2016, MNRAS, 460, 1500

Tartaglia L. et al., 2017, ApJ, 836, L12

Taubenberger S. et al., 2019, MNRAS, 488, 5473

Terreran G. et al., 2016, MNRAS, 462, 137

Tinyanont S. et al., 2016, ApJ, 833, 231

Tonry J., Denneau L., Stalder B., Heinze A., Sherstyuk A., Rest A., Smith K. W., Smartt S. J., 2016, Astron. Telegram, 9526, 1

Tsvetkov D. Y., Volkov I. M., Baklanov P., Blinnikov S., Tuchin O., 2009, Perem. Zvezdy, 29, 2

van Driel W. et al., 1993, PASJ, 45, L59

Vazdekis A., Sánchez-Blázquez P., Falcón-Barroso J., Cenarro A. J., Beasley M. A., Cardiel N., Gorgas J., Peletier R. F., 2010, MNRAS, 404, 1639

Wang L. J. et al., 2017, ApJ, 837, 128

Wiseman P. et al., 2020a, MNRAS, 495, 4040

Wiseman P. et al., 2020b, MNRAS, 492, 2575

Woosley S. E., 2010, ApJ, 719, L204

Woosley S. E., Pinto P. A., Hartmann D., 1989, ApJ, 346, 395

Woosley S. E., Langer N., Weaver T. A., 1993, ApJ, 411, 823

Yaron O., Gal-Yam A., 2012, PASP, 124, 668

Yoshii Y. et al., 2003, ApJ, 592, 467

Zhou X., 1993, IAU Circ., 5782, 2

## SUPPORTING INFORMATION

Supplementary data are available at *MNRAS* online.

**Appendix A.** Mosfit Details (Supplementary Material)

Please note: Oxford University Press is not responsible for the content or functionality of any supporting materials supplied by the authors.

Any queries (other than missing material) should be directed to the corresponding author for the article.

[1]*School of Physics and Astronomy, University of Southampton, Southampton SO17 1BJ, UK*

[2]*DISCnet Centre for Doctoral Training, University of Southampton, Southampton SO17 1BJ, UK*

[3]*Institute of Cosmology and Gravitation, University of Portsmouth, Portsmouth PO1 3FX, UK*

[4]*CENTRA, Instituto Superior Técnico, Universidade de Lisboa, Av. Rovisco Pais 1, PL-1049-001 Lisboa, Portugal*

[5]*The Research School of Astronomy and Astrophysics, Australian National University, Canberra, ACT 2601, Australia*

[6]*Departamento de Física Teórica y del Cosmos, Universidad de Granada, E-18071 Granada, Spain*

[7]*INAF, Astrophysical Observatory of Turin, I-10025 Pino Torinese, Italy*

[8]*Centre for Astrophysics and Supercomputing, Swinburne University of Technology, Hawthorn, Victoria 3122, Australia*

[9]*Sydney Institute for Astronomy, School of Physics, A28, The University of Sydney, NSW 2006, Australia*

[10]*Université Clermont Auvergne, CNRS/IN2P3, LPC, F-63000 Clermont-Ferrand, France*

[11]*School of Mathematics and Physics, University of Queensland, Brisbane, QLD 4072, Australia*

[12]*McDonald Observatory, The University of Texas at Austin, Fort Davis, TX 79734, USA*

[13]*Cerro Tololo Inter-American Observatory, NSF's National Optical-Infrared Astronomy Research Laboratory, Casilla 603, La Serena, Chile*

[14]*Departamento de Física Matemática, Instituto de Física, Universidade de São Paulo, CP 66318, São Paulo, SP, 05314-970, Brazil*

[15]*Laboratório Interinstitucional de e-Astronomia – LIneA, Rua Gal. José Cristino 77, Rio de Janeiro, RJ – 20921-400, Brazil*

[16]*Instituto de Fisica Teorica UAM/CSIC, Universidad Autonoma de Madrid, E-28049 Madrid, Spain*

[17]*CNRS, UMR 7095, Institut d'Astrophysique de Paris, F-75014 Paris, France*

[18]*Sorbonne Universités, UPMC Univ Paris 06, UMR 7095, Institut d'Astrophysique de Paris, F-75014 Paris, France*

[19]*Department of Physics and Astronomy, Pevensey Building, University of Sussex, Brighton BN1 9QH, UK*

[20]*Department of Physics and Astronomy, University College London, Gower Street, London WC1E 6BT, UK*

[21]*Instituto de Astrofisica de Canarias, E-38205 La Laguna, Tenerife, Spain*

[22]*Universidad de La Laguna, Dpto. Astrofísica, E-38206 La Laguna, Tenerife, Spain*

[23]*Department of Astronomy, University of Illinois at Urbana-Champaign, 1002 W. Green Street, Urbana, IL 61801, USA*

[24]*National Center for Supercomputing Applications, 1205 West Clark St, Urbana, IL 61801, USA*

[25]*Institut de Física d'Altes Energies (IFAE), The Barcelona Institute of Science and Technology, Campus UAB, E-08193 Bellaterra (Barcelona), Spain*

[26]*INAF – Osservatorio Astronomico di Trieste, via G. B. Tiepolo 11, I-34143 Trieste, Italy*

[27]*Institute for Fundamental Physics of the Universe, Via Beirut 2, I-34014 Trieste, Italy*

[28]*Observatório Nacional, Rua Gal. José Cristino 77, Rio de Janeiro, RJ – 20921-400, Brazil*

[29]*Centro de Investigaciones Energéticas, Medioambientales y Tecnológicas (CIEMAT), E-28040 Madrid, Spain*

[30]*Department of Physics, IIT Hyderabad, Kandi, Telangana 502285, India*

[31]*Fermi National Accelerator Laboratory, PO Box 500, Batavia, IL 60510, USA*

[32]*Santa Cruz Institute for Particle Physics, Santa Cruz, CA 95064, USA*

[33]*Institute of Theoretical Astrophysics, University of Oslo. PO Box 1029 Blindern, NO-0315 Oslo, Norway*

[34]*Institut d'Estudis Espacials de Catalunya (IEEC), E-08034 Barcelona, Spain*

[35]*Institute of Space Sciences (ICE, CSIC), Campus UAB, Carrer de Can Magrans, s/n, E-08193 Barcelona, Spain*

[36]*Kavli Institute for Cosmological Physics, University of Chicago, Chicago, IL 60637, USA*

[37]*Department of Physics, Stanford University, 382 Via Pueblo Mall, Stanford, CA 94305, USA*

[38]*Kavli Institute for Particle Astrophysics and Cosmology, PO Box 2450, Stanford University, Stanford, CA 94305, USA*

[39]*SLAC National Accelerator Laboratory, Menlo Park, CA 94025, USA*

[40]*Faculty of Physics, Ludwig-Maximilians-Universität, Scheinerstr. 1, D-81679 Munich, Germany*

[41]*Max Planck Institute for Extraterrestrial Physics, Giessenbachstrasse, D-85748 Garching, Germany*

[42]*Universitäts-Sternwarte, Fakultät für Physik, Ludwig-Maximilians Universität München, Scheinerstr. 1, D-81679 München, Germany*

[43]*Australian Astronomical Optics, Macquarie University, North Ryde, NSW 2113, Australia*

[44]*Lowell Observatory, 1400 Mars Hill Rd, Flagstaff, AZ 86001, USA*

[45]*Center for Cosmology and Astro-Particle Physics, The Ohio State University, Columbus, OH 43210, USA*

[46]*Department of Physics, The Ohio State University, Columbus, OH 43210, USA*

[47]*George P. and Cynthia Woods Mitchell Institute for Fundamental Physics and Astronomy, and Department of Physics and Astronomy, Texas A&M University, College Station, TX 77843, USA*

[48]*Department of Astronomy, The Ohio State University, Columbus, OH 43210, USA*

[49]*Radcliffe Institute for Advanced Study, Harvard University, Cambridge, MA 02138, USA*

[50]*Institució Catalana de Recerca i Estudis Avançats, E-08010 Barcelona, Spain*

[51]*Physics Department, 2320 Chamberlin Hall, University of Wisconsin-Madison, 1150 University Avenue, Madison, WI 53706-1390, USA*

[52]*Institute of Astronomy, University of Cambridge, Madingley Road, Cambridge CB3 0HA, UK*

[53]*Department of Astrophysical Sciences, Princeton University, Peyton Hall, Princeton, NJ 08544, USA*

[54]*Department of Physics and Astronomy, University of Pennsylvania, Philadelphia, PA 19104, USA*

[55]*Department of Physics, University of Michigan, Ann Arbor, MI 48109, USA*

[56]*Computer Science and Mathematics Division, Oak Ridge National Laboratory, Oak Ridge, TN 37831, USA*

This paper has been typeset from a TEX/LATEX file prepared by the author.